

## RESEARCH ARTICLE

10.1002/2017JC013712

## Observed Characteristics and Vertical Structure of Mesoscale Eddies in the Southwest Tropical Pacific

Lydia Keppler<sup>1,2,3</sup> , Sophie Cravatte<sup>4</sup> , Alexis Chaigneau<sup>4</sup> , Cori Pegliasco<sup>4</sup> , Lionel Gourdeau<sup>4</sup> , and Awneesh Singh<sup>1</sup>

## Key Points:

- Mean surface characteristics of eddies are described in the Southwest Pacific and their vertical structure is reconstructed by Argo floats
- In the Coral Sea, anticyclonic eddies trap and transport waters in the upper thermocline
- South of  $\sim 20^{\circ}\text{S}$ , eddies are ubiquitous and long-lived, and contribute to the mixing in the lower thermocline

## Correspondence to:

L. Keppler  
lydia.keppler@mpimet.mpg.de

## Citation:

Keppler, L., Cravatte, S., Chaigneau, A., Pegliasco, C., Gourdeau, L., & Singh, A. (2018). Observed characteristics and vertical structure of mesoscale eddies in the southwest tropical Pacific. *Journal of Geophysical Research: Oceans*, 123, 2731–2756. <https://doi.org/10.1002/2017JC013712>

Received 15 DEC 2017

Accepted 27 MAR 2018

Accepted article online 6 APR 2018

Published online 20 APR 2018

<sup>1</sup>The University of the South Pacific (USP), PaCE-SD, Suva, Fiji, <sup>2</sup>The Max-Planck-Institute for Meteorology, The Ocean in the Earth System, Hamburg, Germany, <sup>3</sup>International Max Planck Research School on Earth System Modelling (IMPRS-ESM), Hamburg, Germany, <sup>4</sup>LEGOS, Université de Toulouse, IRD, CNES, CNRS, UPS, Toulouse, France

**Abstract** In the Southwest Pacific Ocean, waters transit from the subtropical gyre before being redistributed equatorward and poleward. While the mean pathways are known, the contribution to the mixing and transport of the water from mesoscale eddies has not been comprehensively investigated. In this research, satellite altimetry data, combined with an eddy detection and tracking algorithm is used to investigate the distribution and surface characteristics of mesoscale eddies in this region of complex bathymetry ( $10^{\circ}\text{S}$ – $30^{\circ}\text{S}$ ,  $140^{\circ}\text{E}$ – $190^{\circ}\text{E}$ ). Detected eddies are then colocalized with in situ data from Argo floats to determine their vertical structure and the effect of eddies on the water masses. The numerous islands affect the eddy behavior as most eddies are formed in the lee of islands, propagate westward and decay when encountering shallow bathymetry. Eddies are sparse and short-lived in the tropical area north of Fiji, impacting only the top 200 meters of water. They do not appear to be able to trap and transport waters in this region. In the Coral Sea, a region of lateral shear between currents transporting waters of different origins, eddies are more numerous and energetic. They affect the water properties down to at least 500 m depth, and anticyclonic eddies trap water to  $\sim 200$  m, contributing to the upper thermocline waters mixing and transport. South of New Caledonia, mesoscale eddies are ubiquitous, with typical lifetimes longer than 5 months. They affect the temperature, salinity, and velocities down to  $\sim 1,000$  m depth, and weakly contribute to the mixing of lower thermocline waters.

## 1. Introduction

The Southwest Tropical Pacific Ocean (SWTP,  $10^{\circ}\text{S}$ – $30^{\circ}\text{S}$ ,  $140^{\circ}\text{E}$ – $190^{\circ}\text{E}$ , Figure 1) is on the pathway of a major oceanic route, redistributing waters from subtropical and higher latitudes toward both the equator and the pole (Fine et al., 1994; Qu & Lindstrom, 2002, 2004). It is also a region of complex bathymetry, with numerous islands and ridges (e.g., the Fiji and Vanuatu archipelagos and New Caledonia) acting as obstacles for the large-scale westward South Equatorial Current (SEC; Figure 1a). The SEC, which is the main westward flow entering the SWTP and extends from the surface to the thermocline, divides into several westward zonal jets when encountering island chains, and bifurcates into two branches when approaching the Australian east coast at  $\sim 20^{\circ}\text{S}$ . The equatorward branch flows through the Solomon Sea, ultimately feeding the western equatorial current system, in particular the Equatorial Undercurrent (Grenier et al., 2011, 2014), and potentially influencing the water properties downstream (Grenier et al., 2013; Qin et al., 2015, 2016). The poleward branch forms the East Australian Current (EAC), a strong western boundary current influencing the regional climate of southern Australia and New Zealand (e.g., Sprintall et al., 1995), and connecting the South Pacific subtropical gyre with the Indian Ocean (Cai, 2006; Ridgway & Dunn, 2007; van Sebille et al., 2014).

The relatively complex circulation of the SWTP and its variability, associated with water mass transformations and mixing during the water transit in the region, can thus have remote climatic effects. As such, this circulation has been extensively studied recently, in particular in the frame of the international Southwest Pacific Ocean Circulation and Climate Experiment (SPICE) program (Ganachaud et al., 2014). The mean circulation in the upper 1,000 m of the SWTP can be summarized as follows (Ceccarelli et al., 2013; Ganachaud et al., 2014; Kessler & Cravatte, 2013b; Ridgway et al., 2002). Most surface and subsurface currents in the region flow westward and extend deep (blue arrows in Figure 1a), with the exception of some

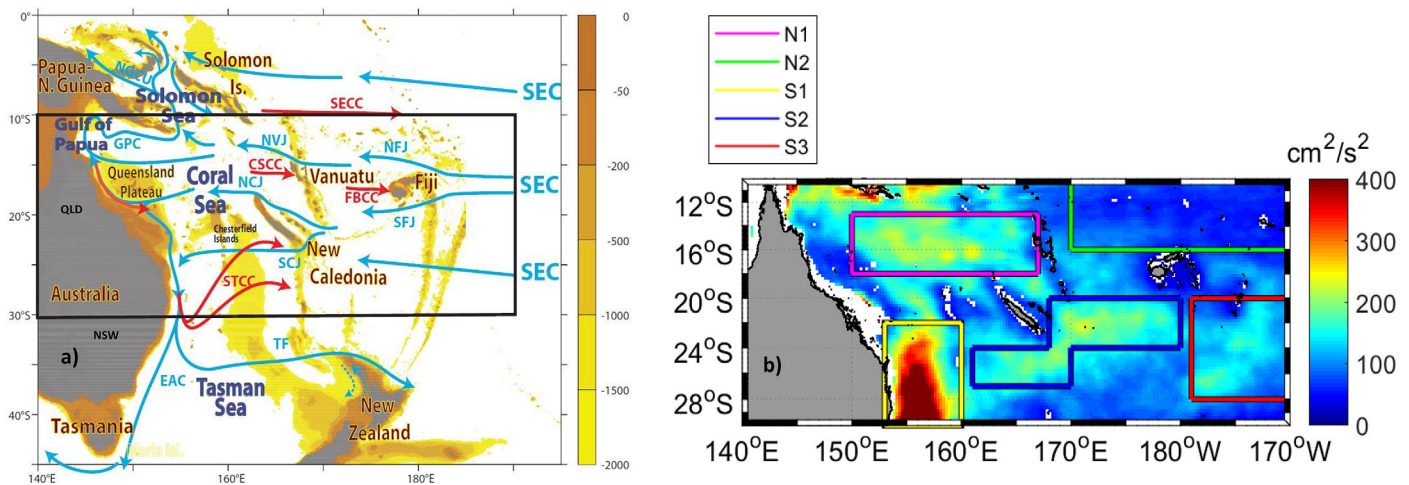


**Figure 1.** Schematic large-scale circulation and eddy kinetic energy in the Southwest Pacific. (a) Bathymetry (in m) of the Southwest Pacific (color shading), showing only depths less than 2,000 m. The Queensland (QLD) and New South Wales (NSW) coasts are shown, in addition to the main currents integrated from 0 to 1,000 m (blue arrows) and surface-trapped counter-currents, only shown when they are different from the subsurface currents (red arrows). The study region is delimited by a black rectangle. The main currents are the SEC: South Equatorial Current; NVJ: North Vanuatu Jet; NCJ: North Caledonian Jet; SCJ: South Caledonian Jet; GPC: Gulf of Papua Current; NGCU: New Guinea Coastal Undercurrent; EAC: East Australia Current; TF: Tasman Front and the surface-only currents are the STCC: South Pacific Subtropical Counter Current; CSSC: Coral Sea Counter Current; FBCC: Fiji Basin Counter Current; and SECC: South Equatorial Counter Current. Adapted from Ganachaud et al. (2014) (b) Map of the mean total EKE (in  $\text{cm}^2 \text{s}^{-2}$ ), filtered with a high-pass Hanning filter at 180 days. White regions are shallower than 200 m. Five dynamically different subregions used in this study are demarcated with colored shapes. See in-text description of these regions.

countercurrents at the surface flowing eastward (red arrows in Figure 1a). The westward SEC splits into a series of westward zonal currents when encountering islands (Figure 1a): the North and South Fiji Jets (NFJ and SFJ, respectively), the broad surface-intensified North Vanuatu Jet (NVJ), the narrow North Caledonian Jet (NCJ) extending to 1,000 m or deeper (Couvelard et al., 2008; Gourdeau et al., 2008), and the subsurface South Caledonian Jet (SCJ) (Ganachaud et al., 2008). In the lee of the Vanuatu archipelago, the surface Coral Sea Countercurrent (CSCC) flows eastward along  $15^\circ\text{S}$  to  $16^\circ\text{S}$ , inducing vertical shears with the underlying westward thermocline circulation (Qiu et al., 2009). When approaching the Australian east coast, the NVJ and part of the NCJ turn northward to form the Gulf of Papua Current (GPC) (Kessler & Cravatte, 2013b), which enters into the Solomon Sea where it merges with the NVJ and forms the equatorward New Guinea Coastal Undercurrent (NGCU) (Cravatte et al., 2011; Davis et al., 2012; Gasparin et al., 2012; Germaineaud et al., 2016). Another part, the SCJ, turns southward to feed into the EAC, which separates from Australia between  $30^\circ\text{S}$  and  $34^\circ\text{S}$  and flows eastward as the Tasman Front (Ridgway & Dunn, 2003). North of this separation area, a series of eastward surface currents also emanates from the EAC recirculation, forming the branches of the upper South Pacific Subtropical Countercurrent (STCC).

Documenting the variability of the transport and water mass properties through the region is crucial to understand the variability of the redistribution of waters toward the equator and poleward. The currents strongly vary at seasonal and inter-annual timescales (e.g., Davis et al., 2012; Holbrook et al., 2005, 2011; Kessler & Cravatte, 2013a; Kessler & Gourdeau, 2007; Ridgway & Godfrey, 1997), but the dominant variability is found at intra-seasonal timescales where mesoscale eddies account for most of the surface eddy kinetic energy (EKE) (Cravatte et al., 2015; Qiu et al., 2009). Indeed, the SWTP is a region with elevated EKE compared to the rest of the tropical and subtropical Pacific, with particularly enhanced EKE in the STCC, the CSCC, and the area of the meandering EAC region (Figure 1b) (Qiu et al., 2009). The strongly sheared mean currents and the presence of numerous islands and complex topography favor the generation of instabilities and mesoscale eddies. The SEC core deepens with increasing latitude, while the near-surface current becomes eastward, or remains westward but weaker than the deeper westward flow (Kessler & Cravatte, 2013b). The western boundary currents also have subsurface velocity maxima, with weaker or opposite surface flow, leading to strong vertical shears and baroclinic instabilities. The proximity of narrow eastward and westward currents also results in significant horizontal shears, favoring the generation of barotropic instabilities.

Previous studies in the Southwest Pacific have mostly focused on the EKE as inferred from altimetry (Qiu & Chen, 2004; Qiu et al., 2009). To our knowledge, the occurrence and properties of coherent mesoscale eddy

structures (Chelton et al., 2011), have not been investigated specifically with observations, except in the EAC region, where large eddies impacting physics and ecosystems have attracted much attention (Brassington et al., 2011; Everett et al., 2012; Mata et al., 2006; Rykova & Oke, 2015; Suthers et al., 2011), and during synoptic cruises (Rousselet et al., 2016). Yet, investigating the generation, properties, and vertical structures of the mesoscale eddies in the whole region is important for several reasons. Firstly, eddies are coherent linear or non-linear structures which may trap water and transport them along their trajectories, affecting the horizontal and vertical distributions of physical and biogeochemical seawater properties from their formation regions to their dissipation sites (Chaigneau et al., 2011; Chelton et al., 2011; Dong et al., 2014; Zhang et al., 2014). They may contribute to the mixing of different water masses during their transit in the region (Rousselet et al., 2016). Hence, it is important to better quantify the effect of eddies in this region of water redistributions. Secondly, transient mesoscale eddies can mask the presence of the mean currents at any given instant and severely bias the transport estimations obtained from synoptic cruise data or glider sections (Cravatte et al., 2015; Kessler & Cravatte, 2013a). Being able to deconvolute the effect of the eddies on a vertical synoptic section would be valuable. Lastly, documenting eddy generation, behavior, and decay in this region of particularly complex topographic obstacles and instabilities is challenging. Unresolved key questions are on the typical vertical extent of these mesoscale structures, the depth to which they affect the water mass properties and large-scale currents, their interactions with islands, and their contribution to the total heat and salt transports. A modeling study using a high-resolution numerical simulation in the Coral Sea (Hristova et al., 2014) investigated the vertical structure of EKE and suggested that the vertical extent of eddies varies within the region. In their model, large eddies tend to span at least the top 600 m of the water column in the Gulf of Papua. These findings would need to be confirmed by observations: misrepresented physics, inexact bathymetry, and boundary conditions of the model may lead to biases in the simulation of eddy properties and vertical extent.

Consequently, the objectives of this paper are to characterize the mesoscale eddies in the SWTP with observations, to infer their signatures on temperature, salinity, velocity, and ultimately their impact on water masses and transports. This study first aims to describe the general distribution, statistics, generation, and decay of the observed mesoscale eddies, based on satellite altimetry and an eddy detection and tracking method (Chaigneau et al., 2008, 2009; Pegliasco et al., 2015). Particular attention is devoted to their behavior when they encounter the numerous islands of the region. Most previous studies on mesoscale eddy variability in this region focused on EKE at the surface, while this study also aims to characterize the vertical structure in the water column by colocalization of altimetry data and Argo float profiles that surface into anticyclonic (AE) or cyclonic (CE) eddies. This method has been extensively used in various regions (e.g., Amores et al., 2017; Castelao, 2014; Chaigneau et al., 2011; Frenger et al., 2015; Pegliasco et al., 2015; Schütte et al., 2016; Souza et al., 2011; Yang et al., 2013; Yang et al., 2015). In each region, the eddy vertical structure varies, being surface-intensified and confined to the upper 100 m layer, or exhibiting a subsurface maximum, depending on the background stratification and generation mechanisms, confirming the importance of regionally focused studies. Attempts have been made to infer a universal eddy vertical structure, using a stretched vertical coordinate depending on the background stratification and the Coriolis parameter (Zhang et al., 2013). Such an approach is useful for inferring the impact of eddies on transports and the climate globally (Zhang et al., 2014), but may not be suitable for inferring regional impacts.

Section 2 describes the data and methods used. The main surface characteristics of the detected eddies including their life cycles, as well as their links with the surface EKE are discussed in section 3. Their vertical structures are described in section 4, where composites of the vertical temperature, salinity, and geostrophic velocity are shown for five dynamically distinct subregions, along with the average trapping depths of AE and CE in these subregions. Finally, the implications of our results are discussed and summarized in section 5.

## 2. Data and Methods

### 2.1. Aviso Satellite Altimetry and Eddy Detection Algorithm

Daily sea-level anomaly (SLA) maps from the Aviso Ssalto-Duacs 2014 altimetry product (<https://www.aviso.altimetry.fr>) between January 1993 and May 2014 are used to automatically identify and characterize mesoscale eddies (~20 km to several hundred kilometers) in the study region (142°E to 170°W and 10°S to 30°S,

Figure 1). This product is based on sea surface height (SSH) measurements taken from multi-mission altimeters. The sea level anomalies (SLA) are referenced to the mean SSH between January 1993 and December 2012 (20 years). The processing and distribution of this product is conducted by the European Copernicus Marine Environment Monitoring Service (CMEMS). In the final product, the daily SLA maps are distributed on a  $0.25^\circ \times 0.25^\circ$  Cartesian grid.

Mesoscale eddies are detected on these SLA maps, using the SLA-based eddy detection algorithm developed by Chaigneau et al. (2009). This algorithm finds local extrema of SLA (maxima for AE, minima for CE) as possible eddy centers, and defines the outermost closed SLA contour around these extrema as eddy edges (Figures 2a and 2b). Note that the edge does not correspond to a specific SLA value and the SLA at the eddy edge varies among the eddies. Chelton et al. (2011) used a similar detection algorithm for their global study on mesoscale eddies, applied to a lower-resolution altimetric product, retaining only long-lived eddies, with large land masks around islands and allowing multiple extrema within a single contour line. Their data set is thus not optimal for our study region, which contains many islands. Multiple studies have shown that SLA-based methods which use the geometrical or “winding-angle method” tend to be more accurate in detecting eddies than other commonly used algorithms (e.g., Chaigneau et al., 2008; Chelton et al., 2011; Souza et al., 2011).

For each detected eddy, several eddy properties are assessed. In our study, the eddy center is defined as the point where the SLA extremum is observed, while the centroid corresponds to the geometrical barycenter of the eddy contour (Figure 2b). The amplitude is defined as the absolute value of the difference between the SLA at the eddy center and the SLA along the eddy edge. The amplitude is therefore positive for both AE and CE. Only eddies with amplitudes larger than 2 cm are retained due to the accuracy of the SLA product described in its documentation (<https://www.aviso.altimetry.fr>). The eddy radius corresponds to the radius of a disk, which covers an equivalent area as the region within the eddy edge (Figure 2b). Only eddies covering at least 4 connected grid points are retained, which corresponds to a minimum radius of  $\sim 20$  km. The EKE was computed as the average EKE inside an eddy, based on the velocity components:

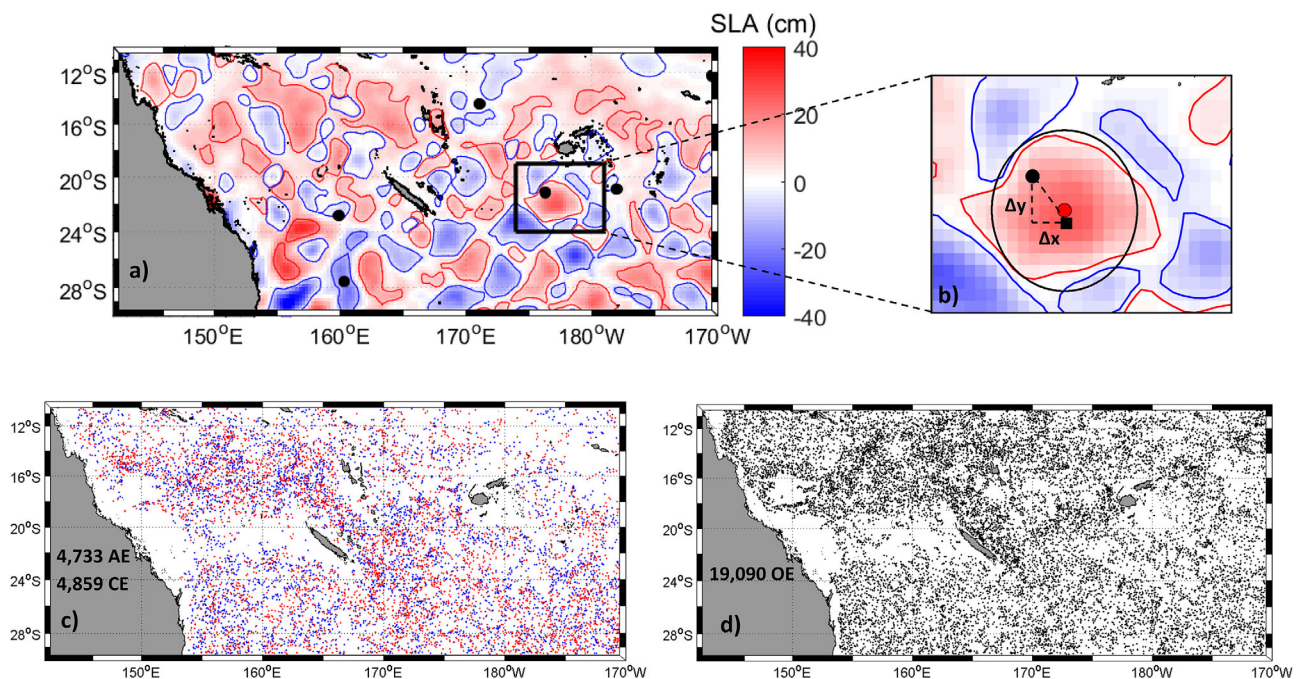


**Figure 2.** Eddy detection algorithm, definitions, and classification of Argo profiles. (a) SLA on 07<sup>th</sup> January 2005 from Aviso on a  $0.25^\circ \times 0.25^\circ$  grid. Detected eddy edges are shown in red (AE) and blue (CE) contour lines and Argo floats that surfaced on the same day are shown as black filled circles. (b) Illustration of the eddy characteristics and floats' positions (black filled circle) relative to the corresponding eddy centers (black filled square); the eddy centroid (red filled circle) and the equivalent circle of radius (black solid line) are also shown. The relative positions of the floats to the eddy center are shown with  $\Delta x$  and  $\Delta y$ . (c) Location of Argo floats that surfaced into AE (red) and CE (blue) between 1<sup>st</sup> January 2003 and 1<sup>st</sup> May 2014. (d) Same as (c) but for Argo floats surfacing outside eddies (OE). The numbers of profiles that surfaced into AE, CE, and OE are indicated over Australia.

$$\text{EKE} = \frac{1}{2} (u'^2 + v'^2) \quad (1)$$

where  $u'$  and  $v'$  are computed from SLA gradients as:

$$u' = -\frac{g}{f} \frac{\Delta \text{SLA}}{\Delta y}; \quad v' = \frac{g}{f} \frac{\Delta \text{SLA}}{\Delta x} \quad (2)$$

and are filtered with a high-pass Hanning filter at 180 days. Furthermore,  $f$  is the Coriolis parameter and  $g$  the standard acceleration due to gravity.

In the next step, the retained eddies are temporally tracked from their genesis to their dissipation using the algorithm developed by Pegliasco et al. (2015). This algorithm works as follows: firstly, if an eddy at time  $t$  overlaps with an eddy of the same polarity (AE or CE) at time  $t + 1$ , they are considered as part of the same trajectory. Secondly, if an eddy at time  $t$  overlaps with several eddies of the same polarity at time  $t + 1$ , a cost function depending on the differences in terms of amplitude, radius, and EKE is computed between the eddy at time  $t$  and the eddies at time  $t + 1$ . The eddy at time  $t + 1$  that minimizes the cost function and is hence the most similar in terms of amplitude, radius, and EKE, belongs to the same trajectory. Thirdly, if no overlapping is found with eddies at time  $t + 1$ , the same procedure is conducted for time  $t + 2$ . If there is still no intersection after two days, the eddy at time  $t$  is considered as dissipated (see Pegliasco et al., 2015, for a more detailed description). In order to consider only coherent eddies and avoid small-scale noisy structures, in addition to the mentioned filters on eddy size (minimum amplitude of 2 cm and radius of  $\sim 20$  km), we only retain eddies with a minimum lifetime of 14 days and with a median radius of at least 50 km along their trajectories. The method of using the median radius along the trajectory better represents eddies that grow and shrink above and below a certain threshold throughout their trajectories. Indeed, removing individual eddies with radii smaller than 50 km on the daily SLA maps would result in many trajectories being falsely broken up into multiple shorter-lived eddies.

It is worth noting that both the SLA gridded product, based on an interpolation of satellite tracks, and the detection algorithm have limitations. The repeat cycle of the different altimeters used in the merged product varies between 10 and 35 days, and the gaps between ground tracks lead to errors in the SLA fields (Pilo et al., 2015) being heavily interpolated to produce a daily  $0.25^\circ \times 0.25^\circ$  grid. Thus, the detection method can identify erroneous eddies; eddies can also be lost by the tracking method, and thus be counted twice, because of the spatiotemporal gaps in the gridded products. Several configurations of the algorithm with different minimum radii and minimum lifetimes have been tested, and the choices made correspond to the best compromise between keeping and losing what we consider as real features.

The final eddy data set consists of 13,799 eddy trajectories, almost equally distributed between AE (6,756) and CE (7,043). These trajectories correspond to  $\sim 480,000$  AE and  $\sim 520,000$  CE when counting each individual eddy detected on the daily SLA maps.

## 2.2. Argo Data and Colocalization

In order to determine the eddies' vertical structures, vertical temperature and salinity profiles acquired by Argo floats between 1 January 2003 and 1 May 2014 are used (Argo, 2000). Only profiles flagged as "good" or "probably good" are retained for the analysis. This delayed-time data set consists of 28,682 vertical profiles in the study region. Argo profiles are densely distributed throughout the SWTP (Figures 2c and 2d), with only small gaps in areas shallower than 1,000 m, where the floats cannot successfully complete their descent and drift at their nominal parking depth. These regions are especially prominent near the coasts and include the shelf off the Australian east coast and the area west of New Caledonia (Figures 2c and 2d). The number of available profiles increased with time since the start of the Argo program, leading to an enhanced sampling toward the end of the study period, potentially creating a bias toward observations in a warmer period. Specifically, the first profile was on 5 January 2003 and 50% of the profiles were obtained after 9 April 2010, which is approximately 35% of the time period.

Before the analysis, the temperature and salinity data from the Argo profiles were first quality controlled. Outliers (when differences from the climatology were greater than 5 standard deviations) and incomplete profiles (having less than 34 good values in the profile) were removed. Density inversions (greater than  $0.05 \text{ kg m}^{-3}$ ) were also removed. The remaining Argo profiles were then linearly interpolated onto 69 pressure levels

between the surface and 2,000 dbar, with separate levels spaced from 2.5 dbar near the surface to 50 dbar apart at greater depths. The dynamic height was computed for each depth level relative to a reference depth of “no-motion” of 1,850 m. This reference depth was chosen as the assumed level of no motion because many floats had missing values below 1,850 m. It should be noted, however, that there might still be an effect of eddies at 1,850 m. Hence, the currents may be underestimated using this method, as it assumes no motion at this depth. This hypothesis will be further discussed in section 4.3 and the Appendix A.

To determine the different effects of AE and CE on the seawater properties in the water column, Argo profiles are classified into 3 categories depending on whether they surfaced into AE, CE, or outside of eddies (OE) (so-called colocalization, Figures 2c and 2d). Figures 2a and 2b show an example of the Argo floats’ distribution in relation to the eddies for a given day (7 January 2005). On this particular day, one Argo float surfaced into an AE, two floats surfaced into CE, and two surfaced OE. On average and considering all the available Argo floats’ profiles, AE and CE are sampled approximately equally: ~17% of floats surfaced into AE, ~17% into CE and ~66% OE (Figures 2c and 2d).

Temperature and salinity anomalies relative to a mean climatology are computed for each profile. The selected climatology is based on the Roemmich and Gilson (2009)  $0.25^\circ \times 0.25^\circ$  monthly gridded product based on Argo profiles ([http://sio-argo.ucsd.edu/RG\\_Climatology.html](http://sio-argo.ucsd.edu/RG_Climatology.html)). It is interpolated onto the same 69 depth levels between the surface and 2,000 dbar, and extracted at the same time and locations as the corresponding Argo profiles.

Previous studies (e.g., Chaigneau et al., 2011; Willis & Fu, 2008) pointed out that this method is prone to several potential errors and biases. Firstly, as mentioned in section 2.1, the gridded SLA product is expected to show errors. Secondly, as the detected eddies are based on the mean SLA of a day, and not on the exact SLA at the time when the Argo float is at the surface, further errors on the location of the Argo float in relation to eddy are expected (Chaigneau et al., 2011). Chaigneau et al. (2011) estimated in their study region the total error to be on scales of ~1 km, while it could even reach distances of ~5 km. Obviously, this could lead to some profiles being incorrectly classified, especially when the floats surfaced close to the identified eddy edge. Additional errors are likely to be present in the automated eddy detection (e.g., Chaigneau et al., 2011; Willis & Fu, 2008).

Furthermore, it was found that Argo floats tend to surface into larger and more energetic eddies than the average (not shown). The results are therefore expected to be slightly over-estimated.

In addition, the temperature and salinity anomalies computed relative to the climatology are not necessarily representative of the interior eddy conditions. Other variations could explain the departure from the mean. Large-scale inter-annual conditions or internal waves could strongly influence the vertical profiles. In addition, the climatology, which is based on Argo profiles, already contains profiles within AE and CE. As a result, a large number of profiles is needed to infer the mean signature of an eddy, and the dispersion around the mean is not negligible. This is presented and discussed in section 4.

### 2.3. Composite Vertical Structures

As will be explained below, the study region was divided into different subregions based on the surface properties of the eddies. Both one-dimensional (average vertical profiles inside eddies regardless of distance from the eddy center) and two-dimensional composites (average vertical profiles, depending on both the depth and the distance from the eddy center) were computed. The two-dimensional composite structures of the temperature and salinity (T/S) anomalies inside the individual eddies in the different subregions are computed as follows:

1. The distance of the position of the Argo float relative to the eddy center is determined at the surface. The distance is then normalized by the radius of the eddy. A normalized distance of 0 hence corresponds to the eddy center and 1 to the eddy edge (Figure 2b).
2. Assuming isotropy, all observations are used as a function of the normalized distance, regardless of their angle to the eddy center.
3. The observations are mirrored at 0 to obtain more accurate interpolated results near the eddy centers, where only a few observations are available (it is rare that the float surfaces exactly at the eddy center detected from altimetry).

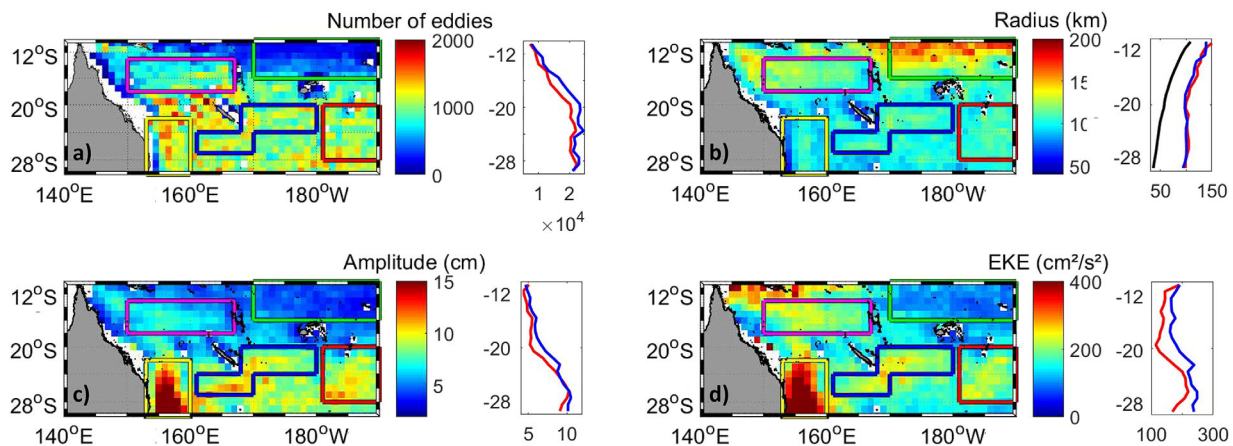


**Figure 3.** Mean eddy characteristics computed on  $1^\circ \times 1^\circ$  grid. (a) Number of eddies; (b) Radius (in km); (c) Amplitude (in cm); (d) EKE (in  $\text{cm}^2 \text{s}^{-2}$ ); White areas are regions shallower than 200 m. The right panel shows the mean values of each parameter as a function of latitude for AE (red) and CE (blue). For the radius, the mean theoretical first mode Rossby radius of deformation for the study region is added in black. The same subregions as in Figure 1 are marked: N1 (magenta), N2 (green), S1 (yellow), S2 (blue), and S3 (red).

- An objective analysis (Barnes, 1973) with a Barnes smoothing length scale of 0.5 for both the x and y sense and 3 Barnes iterations is conducted to interpolate the T/S data onto a regular grid at each depth level. The vertical composites are then computed as a function of depth.

The composite structure of the geostrophic (swirl) velocity is computed based on the dynamic height anomaly composite. The dynamic height anomaly is firstly computed for each profile, relative to 1,850 m (see section 2.2). Next, steps 1 to 4 described above are followed, but instead of step 4, a Gaussian fit is applied to the dynamic height samples at each depth to obtain the dynamic height composite. We recognize that this method assumes an a priori Gaussian structure, which is not necessarily the case, but is a good approximation. This result was found to be much less noisy and more realistic swirl geostrophic velocities relative to 1,850 m were obtained with this method compared to the Barnes (1973) objective analysis. The corresponding absolute swirl geostrophic velocities are finally obtained by adding a constant on the vertical, estimated by comparing the dynamic height anomaly and SLA composites. This method, its validity, and the associated errors are discussed in the Appendix A.

### 3. Eddy Characteristics at the Surface

#### 3.1. Statistics and Eddy Characteristics

The mean surface characteristics of eddies (number of eddies, radius, amplitude, and EKE) are shown in Figure 3.

When considering the study region as a whole, observed eddy characteristics are similar to the findings on global eddies from Chelton et al. (2011): the mean eddy radius in the study region is found to be  $\sim 100$  km, ranging between  $\sim 20$  km and more than 200 km (Table 1 and Figure 3b). Averaged zonally, the mean radius decreases with increasing latitude with a similar slope as the theoretical Rossby radius of deformation

(Figure 3b, side plot), while being much larger, as also noted by Chelton et al. (2011). While eddies have amplitudes between  $\sim 2$  cm and nearly 30 cm in the study region, the mean amplitude is found to be  $\sim 8$  cm, and the median  $\sim 6$  cm (Table 1 and Figure 3c). Note that as mentioned in section 2.1, the eddy amplitude is defined as the absolute value of the difference between the SLA at the eddy center and the SLA at the eddy edge. The map of the EKE within eddies presented in Figure 3d is virtually the same as the map of the mean intra-seasonal EKE (inside and outside of eddies) shown in Figure 1b, confirming that mesoscale eddies account for most of the intra-seasonal EKE. The mean EKE inside eddies is found to be  $\sim 200 \text{ cm}^2 \text{ s}^{-2}$  (Table 1).

**Table 1**  
Dispersion Around the Mean Characteristics of the Eddies

	Mean	Median	25th percentile	75th percentile	Maximum	Minimum
Radius AE (km)	103	96	68	133	231	23
Radius CE (km)	101	94	68	130	224	23
Amplitude AE (cm)	7	6	4	10	24	2
Amplitude CE (cm)	8	6	4	11	29	2
EKE AE ( $\text{cm}^2 \text{ s}^{-2}$ )	174	130	71	238	981	8
EKE CE ( $\text{cm}^2 \text{ s}^{-2}$ )	203	145	76	288	1,200	8

Note. outliers (mean  $\pm 5$  standard deviations were removed).

Eddies and their characteristics are not evenly distributed around the study region, but exhibit a clear latitudinal dependency. There are considerably more eddies toward the south of the study region, and fewer eddies in the northern part, especially east of 165°E, and north of Fiji and Vanuatu archipelagos (Figure 3a). There are also fewer eddies in areas of shallow bathymetry around the Chesterfield Islands and above the Queensland Plateau, and near islands and coasts, including Australia's east coast. Interestingly, there also tend to be fewer eddies above deep ridges, suggesting a potential impact of the bottom topography on the eddy frequencies (Figures 1a and 3a). Although some studies have found that eddies of different polarity can be dominant in different areas (e.g., Yang et al., 2013), no considerable polarity contrasts were observed in this study region (not shown). The only noticeable differences, in line with the global study by Chelton et al. (2011), are that small eddies (radius <50 km) and eddies with large amplitudes (>8 cm) are dominantly cyclonic, while large eddies (radius >150 km) and eddies with small amplitudes (<5 cm) are dominantly anticyclonic (not shown). Consequently, maps of eddy surface properties (Figures 3 and 4) are presented for the whole data set, without differentiating between AE and CE.

Although eddies are present almost in the whole study area, three subregions of high surface EKE stand out, contrasted with two areas of lower EKE, with different eddy properties (Figure 1b). The naming of these subregions is N1-N2 for the northern regions, and S1-S3 for the southern regions:

1. Region S1: The meandering EAC and eastward Tasman Front region (Bowen et al., 2005; Ridgway & Dunn, 2003) in the southwestern part of the study region is the most energetic subregion. The area where the EAC separates from the coast is indeed characterized by intense eddy activity with large eddies north of the separation point (Rykova & Oke, 2015) and the formation of strong AE in the retro-reflection area (Brassington et al., 2011; Everett et al., 2012; Mata et al., 2006; Suthers et al., 2011). Both barotropic and baroclinic instabilities have been suggested to contribute to the growth of eddies in this region. From our detection method, eddies display different characteristics compared to the average global findings. They have a mean amplitude of  $\sim 12$  cm (Figure 3c), and a mean EKE of  $\sim 400$   $\text{cm}^2 \text{s}^{-2}$  (Figure 3d). Their values are significantly higher than in the rest of the SWTP, where eddies have mean amplitudes and EKE of  $\sim 8$  cm and  $200$   $\text{cm}^2 \text{s}^{-2}$ , respectively (Table 1). However, eddies in the EAC do not have larger radii than elsewhere in the study region (Figure 3b).

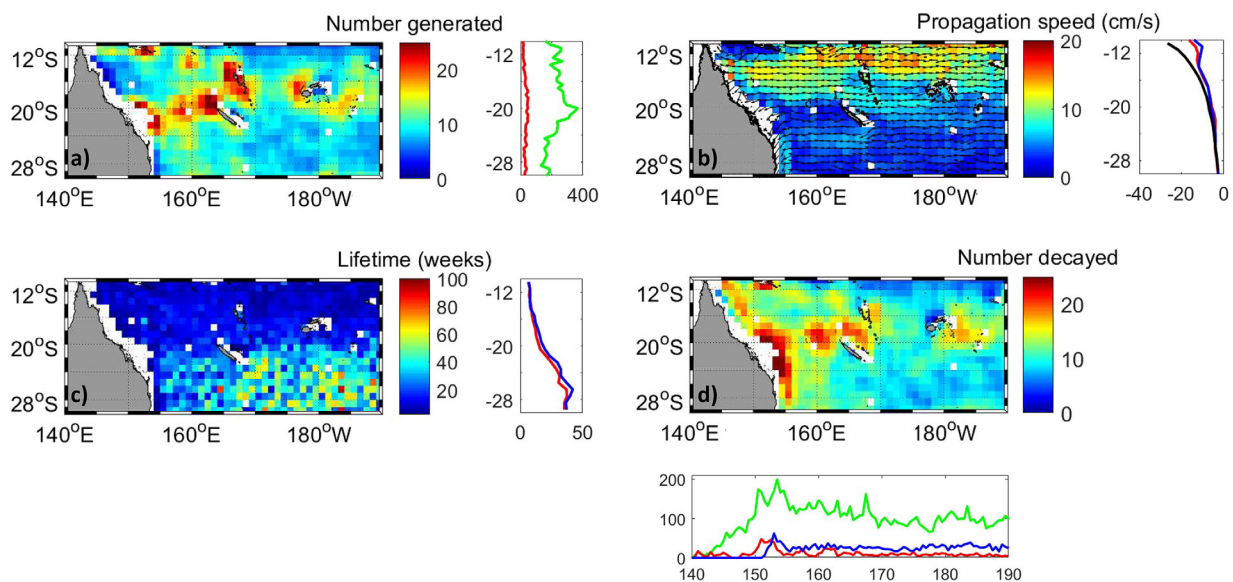


**Figure 4.** The eddy life cycle. (a) Number of eddies (AE and CE) generated on a  $1^\circ \times 1^\circ$  grid, smoothed with a 2D moving average window of  $2^\circ \times 2^\circ$ . The side panel shows the number of eddies generated inside (green) and eastward (red) of the study region as a function of latitude. (b) Mean eddy propagation speed (in color) and direction (vectors). The side panel shows the mean zonal propagation speed for AE (red) and CE (blue), as well as the theoretical long Rossby wave phase speed (black). (c) Median eddy lifetime at the location of their genesis. The side panel shows the mean zonal lifetime speed for AE (red) and CE (blue). (d) Distribution of the number of eddies (AE and CE) decayed, smoothed with a 2D moving average window of  $2^\circ \times 2^\circ$ . The bottom panel shows the number of eddies that decayed inside (green) and North (red) or South (blue) of the study region as a function of longitude. (a-d) White areas are shallower than 200 m.

2. Region S2: South and East of New Caledonia and between 21°S and 29°S is the South Pacific Subtropical Countercurrent (STCC) region, where high surface EKE has been shown to be generated by baroclinic instabilities due to the vertical shear between the eastward-flowing surface STCC and the underlying westward-flowing SCJ (Qiu & Chen, 2004). Using our detection method, we find that eddies in this subregion are more frequent, and clearly larger than north of 20°S, with mean amplitudes of 9 cm (Figure 3c),  $\sim 200 \text{ cm}^2 \text{ s}^{-2}$  EKE (Figure 3d), and radii over 100 km (Figure 3b).
3. Region N1: In the Coral Sea Countercurrent (CSCC) band, around 16°S and west of Vanuatu, the relatively high EKE has been linked to barotropic instabilities due to the horizontal shear between the eastward flowing CSCC and its neighboring westward-flowing NCJ and NVJ (Qiu et al., 2009). Qiu et al. (2009) also noted that positive and negative SLA anomalies in the area propagate westward at a speed of  $0.12 \text{ m s}^{-1}$  and that most of the largest anomalies are locally generated. Our study reveals that eddies in this band are more numerous, and have higher amplitudes than in the same latitude ranges east of Vanuatu ( $\sim 170^\circ\text{E}$ ) (Figures 3a and 3c).

In the Gulf of Papua and at the entrance of the Solomon Sea, high EKE is also observed, probably related to eddies formed by the meanders of the Gulf of Papua boundary current (Hristova et al., 2014) and the interaction of the large-scale circulation with the relatively shallow bathymetry and islands (Figure 1a). This region is not further discussed, as only very few Argo floats surfaced into eddies in this area.

For the rest of the paper, in order to investigate eddy properties in regions with weaker EKE and larger radii, we also define a region N2, east of 165°E, and north of Fiji and Vanuatu archipelagos where eddies are sparse (Figures 1 and 3a). The eddies in this northern region have larger radii ( $\sim 140 \text{ km}$ , Figure 3b) and weaker amplitudes ( $\sim 4 \text{ cm}$ , Figure 3c), resulting in very weak EKE ( $\sim 100 \text{ cm}^2 \text{ s}^{-2}$ , Figure 3d). We also define a region S3 in the southeastern part of the study area, where eddies have similar surface properties as region S2 (Figure 3), but is not an area of known baroclinic instabilities.

### 3.2. The Life Cycle of Eddies: Generation, Propagation, and Decay

The locations of eddy generation (first detection) and decay (last detection) are also investigated. The majority of eddies ( $\sim 88\%$ ) form within the study region while only  $\sim 12\%$  are generated outside and propagate into the region, usually from the east (Figure 4a). Areas just west (in the lee) of the islands of Fiji, Vanuatu, New Caledonia, and even the Chesterfield Islands, stand out as regions where numerous eddies are generated, whereas fewer eddies are generated in the open ocean. This map of eddy genesis is different from the geographical distribution of eddies (Figure 3a). In particular, eddies are more numerous in the southern part of the study region, where fewer eddies are generated. This discrepancy is because the eddies in the southern part of the region propagate slower (Figure 4b) and live much longer (Figure 4c), and thus are more frequent and ubiquitous there. On the contrary, eddies generated west of the islands have shorter lifetimes of a few weeks (Figure 4c) and also weaker amplitudes and smaller radii (Figures 3b and 3c).

The geographical distribution of the eddy genesis is also notably different from that of the EKE distribution (compare Figure 4a with Figure 1b). As discussed in the previous section, there are regions of barotropic and baroclinic instabilities, which are linked to high levels of EKE, but these regions do not coincide with a greater number of newly generated eddies. Region S1 only shows increased levels of genesis toward its northern part (around 22°S, 152°E), while the rest of this region and region S2 does not show increased numbers of eddy genesis. In addition, in region N1, west of Vanuatu, where barotropic instabilities have been suggested to generate high eddy variability (Qiu et al., 2009), Figure 4a does indeed show a significant level of eddy generation. However, this region does not stand out compared to the west coast of islands in the study region, where more eddies are generated. Many eddies generated west of Vanuatu and west of New Caledonia propagate westward and converge there, advected by the mean currents (Figure 4b). During their lifetime, their EKE doubles (not shown); the contribution of the barotropic instabilities to the eddies' energy growth is not known. Further research could be conducted on this to explore the mechanisms involved.

As expected, eddies were found to generally propagate westward (Figure 4b). However, as will be discussed in the next section, they are also interacting with the mean flow, and their westward propagation speed depends on the mean velocity of the large-scale circulation. As the mean flow, they are sometimes deflected northward and southward around islands and shallow bathymetric areas or are affected by other

**Table 2**  
*Dispersion Around the Distance (Between the Location of Genesis and Decay) and Lifetime of Eddies*

	Mean	Median	25th percentile	75th percentile	Maximum	Minimum
Distance AE (km)	327	184	93	381	4,000	23
Distance CE (km)	343	193	100	409	5,073	23
Lifetime AE (weeks)	19	8	3	22	253	2
Lifetime CE (weeks)	20	9	4	26	203	2

(~17%), but most of them (~75%) decay inside the region (bottom panel in Figure 4d). While the median eddy lifetime is ~9 weeks, their mean lifetime is considerably longer with ~20 weeks due to the very long lifetime of some eddies. Such very long-lived eddies include the eddy with the longest lifetime, which was tracked for approximately 5 years (Table 2). This particular eddy was generated at ~175°E, southeast of New Caledonia and stayed between 24°S and 28°S for its entire lifetime, covering a beeline of ~1,600 km between the location of its genesis and its decay close to the Australian east coast.

Eddies tend to live longer in the south (Figure 4c), where they are less subjected to topographic obstacles, and thus dissipation. Some eddies were observed to cross the entire study region, but the mean distance traveled by the eddies is relatively short (~330 km; Table 2). Table 2 also shows that many eddies cover very short distances (median distance ~190 km), while only a few eddies have very long trajectories (maxima of several thousands of kilometers, Table 2). Note that when considering the total length of an eddy trajectory, including the meandering of an eddy, rather than just considering the beeline between the eddy formation and dissipation locations, the mean distances are considerably longer (~800 km, not shown).

Eddies that cover extremely long distances (more than 3,000 km, called long-distance eddies in this section), tend to have slightly higher EKE and amplitude compared to the average. Specifically, the mean EKE of the eddies traveling over long-distances for AE (CE) is approximately 190 (220)  $\text{cm}^2 \text{s}^{-2}$ , while the mean EKE of all eddies lies at approximately 170 (200)  $\text{cm}^2 \text{s}^{-2}$ . Similarly, the mean amplitude of long-distance eddies is approximately 8.7 (8.1) cm, while it is 7.3 (7.8) cm when considering all AE (CE). At the same time, the mean radius of long-distance eddies is not significantly different to the mean radius of all eddies.

factors, such as seamounts. The mean propagation velocity in the study region, computed based on eddy trajectories, is approximately  $7 \text{ cm s}^{-1}$ , with eddies propagating faster with decreasing latitude (Figure 4b). The zonal average of the propagation velocity is similar to the zonal average of the theoretical Rossby wave phase speed in the study region (right panel in Figure 4b), which is in agreement with the findings by Chelton et al. (2011) on global scales.

The majority of eddies decay (or are lost by the tracking method) when encountering the eastern coasts of islands (e.g., the Fiji and Vanuatu archipelagos or New Caledonia), Australia and shallow bathymetry (e.g., surrounding the Chesterfields Islands) (Figure 4d). Few eddies propagate out of the study region toward the north (~8%) or south

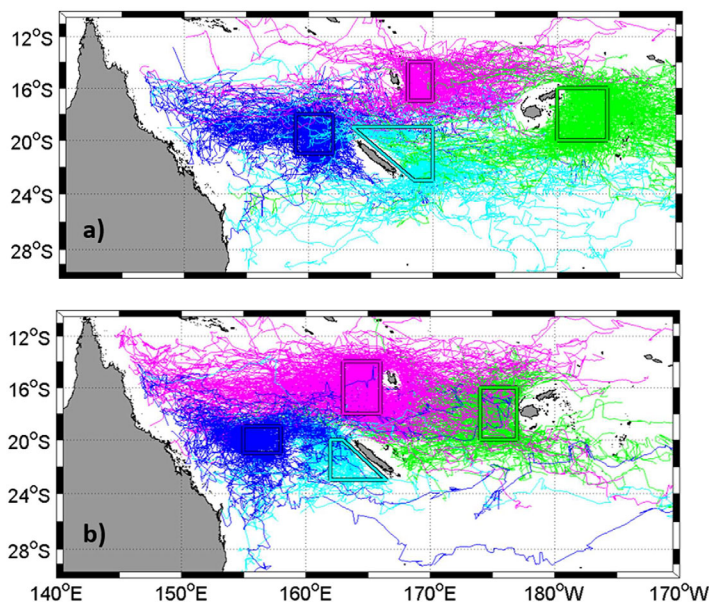


**Figure 5.** Trajectories of eddies which passed through the boxes east (a) or west (b) of large islands and coasts (lines). The colored rectangles delimit the area which the eddies pass and the trajectories are shown in the corresponding color. Blue: Chesterfield Islands; Cyan: New Caledonia; Purple: Vanuatu; Green: Fiji.

### 3.3. Eddy Behavior Around Islands

In the SWTP, mesoscale eddies, as detected by our tracking method, interact strongly with the numerous islands. Figure 5a shows the trajectories of eddies encountering the main island chains (Chesterfield Islands in blue, New Caledonia in cyan, Vanuatu in magenta, Fiji in green) from the east. As revealed by our tracking method, many eddies (46%) decay upon encountering an island from the east (Table 3). However, numerous eddies (54%) also bifurcate southward or northward around the islands, following the mean currents, and few eddies even manage to pass multiple island groups and to cross large parts of the study region.

Note that the large islands (e.g., the main island of New Caledonia and the larger islands of the Fiji and Vanuatu archipelagos) are masked in the altimetric Aviso product, and hence the trajectories have to either decay or bifurcate around them. At the same time, eddies often seem to pass through the smaller islands, which are not masked by the product. Whether this behavior is realistic (eddies with radii larger than islands do not see them) or due to an unrealistic interpolation of the SLA fields around islands, remains to be

**Table 3**  
Percentage of Eddy (AE and CE) Trajectories That Decay Within or Bifurcate Around the Island Regions From Figure 5

	Decay East	Form West
Chesterfield Islands	44%	29%
New Caledonia	32%	39%
Vanuatu	35%	50%
Fiji	61%	44%
Total	46%	43%

elucidated, for example by investigating their behavior in a high-resolution Ocean General Circulation Model (OGCM) with a realistic topography.

Whether or not an island or archipelago tends to cause eddies to decay or move around them does not seem to correlate to the islands' sizes. For example, the Chesterfield Islands are a very small island group (not masked in the altimetric product) but are surrounded by a large region of shallow bathymetry. There, nearly half (44%) of the eddies that move toward this island group from the east decay, while the rest (56%) bifurcates around the archipelago. In the much larger

island groups of New Caledonia and Vanuatu, considerably fewer eddies decay east of the islands (32% and 35%, respectively) than bifurcate around them (68% and 65%, respectively). Eddies that approach Fiji, which is among the largest island groups in the study region, are significantly more likely to decay (61%) than to bifurcate around this archipelago (39%).

In contrast, Figure 5b shows the eddy trajectories that passed through the west of the same island groups, indicating that many eddies that are present west of islands, were formed there (43%, Table 3). Table 3 further specifies that 29% (39%, 50%, 44%) of the eddies that are present west of the Chesterfield Islands (New Caledonia, Vanuatu, Fiji respectively) were formed there. Interestingly, these eddies detected for the first time west of the islands, are not small features decaying rapidly. They do propagate westward on long distances (Figure 5b).

As the surface properties were found to be very diverse in the study region, the next section will discuss the vertical structure in different subregions of distinct eddy dynamics.

## 4. Eddy Vertical Structure

### 4.1. Induced T/S Anomalies in the Water Column

#### 4.1.1. Mean Water Masses and Hydrological Properties

To help understand the eddy signatures on water mass properties, mean vertical meridional sections of temperature and salinity are first shown in the eastern part of our study region (175°E) and in the Coral Sea (162°E) (Figure 6). At both longitudes, surface warm and fresh waters are found north of 16°S. Sea surface temperature drops from nearly 30°C to 22°C between 10°S and 30°S, and the 20°C isotherm, corresponding roughly to the 24.5 kg m<sup>-3</sup> isopycnal that upwells from ~200 m to ~100 m. Deeper isopycnals are lifted toward the north, reflecting the tilted structure of the subtropical gyre, whose bowl is displaced southward with depth (Kessler & Cravatte, 2013b). The mean salinity profile is more complex. At both longitudes, a salinity maximum of 35.6–35.7 is found north of 16°S below the fresh upper layer in the thermocline (on the 24.5 kg m<sup>-3</sup> isopycnal), and is associated with South Pacific Tropical Waters (SPTW) formerly subducted in high evaporation regions (see Grenier et al., 2013, 2014) for a description of their pathways). Below ~800 m depth, a salinity minimum of ~34.4 is found on isopycnal 27.2, associated with the penetration of the Antarctic Intermediate Waters in the whole region. Both the salinity maximum and minimum are progressively eroded as these water masses travel into the southwest Pacific (compare Figures 6b and 6d) (see also Gasparin et al., 2014 and Kessler & Cravatte, 2013b).

#### 4.1.2. Anomalies in the STCC Region (Subregion S2)

Figure 7 shows examples of the average T and S anomalies inside AE and CE within subregion S2, computed by averaging all the vertical profiles acquired within detected eddies (see section 2.2). The average eddy signature is as expected for surface-intensified eddies, with anomalies largely symmetric between AE and CE: waters are downwelled inside AE, resulting in positive temperature anomalies on a depth coordinate profile, while waters are upwelled inside CE, causing negative temperature anomalies in the water column. The observed salinity anomalies are linked to the mean vertical salinity structure. Above the salinity maximum in the thermocline, negative (positive) salinity anomalies are observed within AE (CE) because of the downwelling (upwelling) of fresher (saltier) water in surface-intensified eddies. Below the thermocline, saltier (fresher) water is downwelled (upwelled) inside AE (CE), resulting in positive (negative) salinity anomalies. Below the salinity minimum observed at intermediate depths around 800–1,000 m, a slight negative (positive) anomaly is seen within AE (CE), not significant in this subregion.

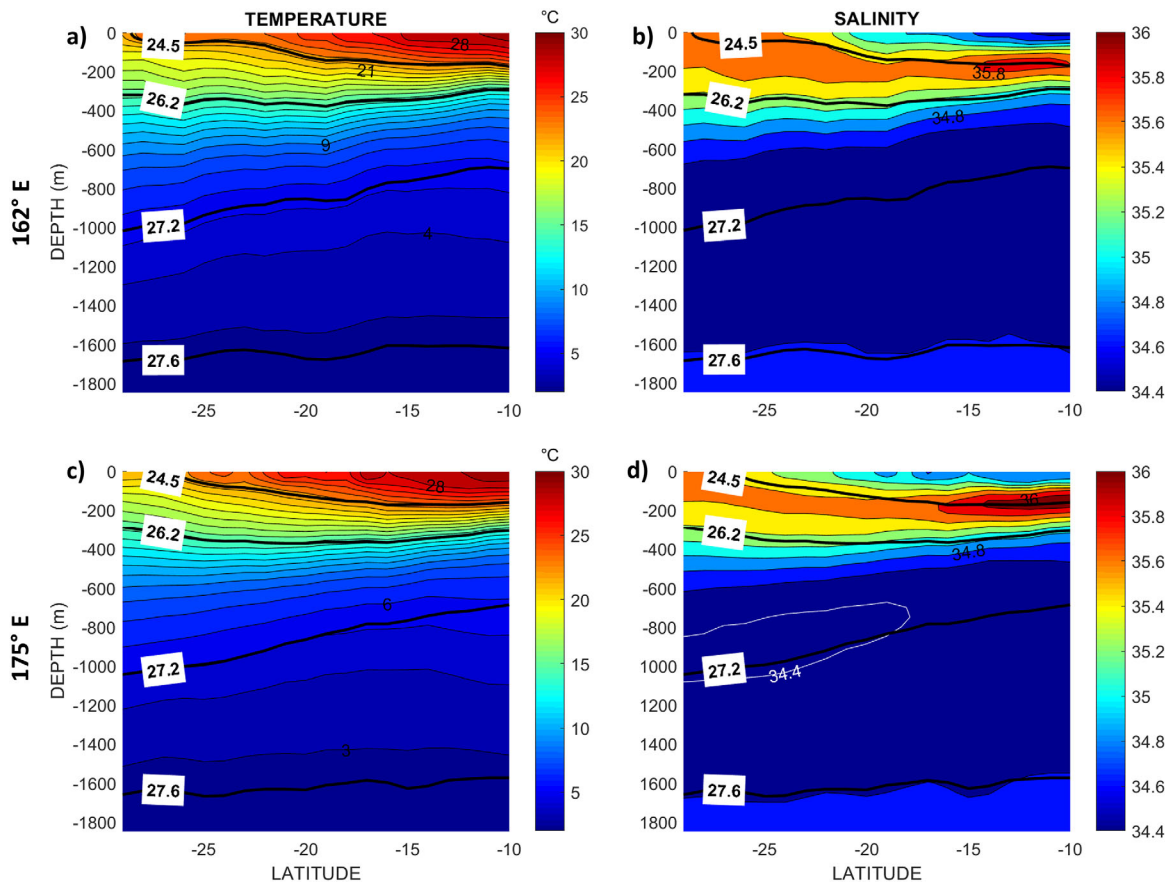


**Figure 6.** Mean (a, c) temperature and (b, d) salinity as a function of latitude and depth along (a, b) 162°E and (c, d) 175°E. Thick black contours show the depths of some key isopycnals. The salinity minimum is marked in white (d).

Large temperature anomalies are observed in this region from the surface to about  $\sim 500$  m depth. The strongest temperature anomalies with typical values of  $\pm 0.7^\circ\text{C}$  are observed at 100 m, at the depth of the thermocline, where the vertical temperature gradient is stronger. Below this depth, anomalies decrease and are reduced to about  $0.1^\circ\text{C}$  at 1,000 m, while still being significant. Similarly, large salinity anomalies are observed up to  $\sim 500$  m depth. The largest salinity anomalies are found below the thermocline and maximum at  $\sim 400$  m, of approximately  $\pm 0.08$ . Outside eddies, mean anomalies are close to zero, validating our method and suggesting the significance of the mean T/S anomalies obtained within eddies.

To highlight the deviation of these anomalies from the average, Figures 7a and 7b shows the standard error around the mean, while Figures 7c and 7d displays the 25<sup>th</sup> and 75<sup>th</sup> percentile around the median. Figures 7c and 7d also reveals that although the average structure displays typical behavior of surface-intensified eddies, they have a large variability as shown by the 25<sup>th</sup> to 75<sup>th</sup> percentile around the median. Many Argo profiles inside AE (CE) even have negative (positive) temperature anomalies. Influences such as large-scale inter-annual variations or high-frequency internal waves could explain the departure from the climatology. Indeed, the region is subject to important inter-annual variability, linked in particular to the El Niño Southern Oscillation (e.g., Holbrook et al., 2005). The SWTP is also known to be a site of relatively strong internal waves (e.g., Ray & Zaron, 2016) that may bias a vertical profile sampled within a few hours. For the readability of the figures, anomaly profiles in other regions are only shown with the standard error (Figure 8).

#### 4.1.3. Contrasts Between Subregions

Figure 8 shows the mean T/S vertical anomaly profiles inside eddies, in the different subregions defined previously, and Figure 9 shows the associated 2D composites to infer the differences within the region. The number of Argo profiles used to compute the mean anomaly profiles is also given in Figure 8. Both figures show that eddies in all subregions have a vertically symmetric structure when comparing AE and CE. This is not always the case, and studies in other regions have often found asymmetries between AE and CE

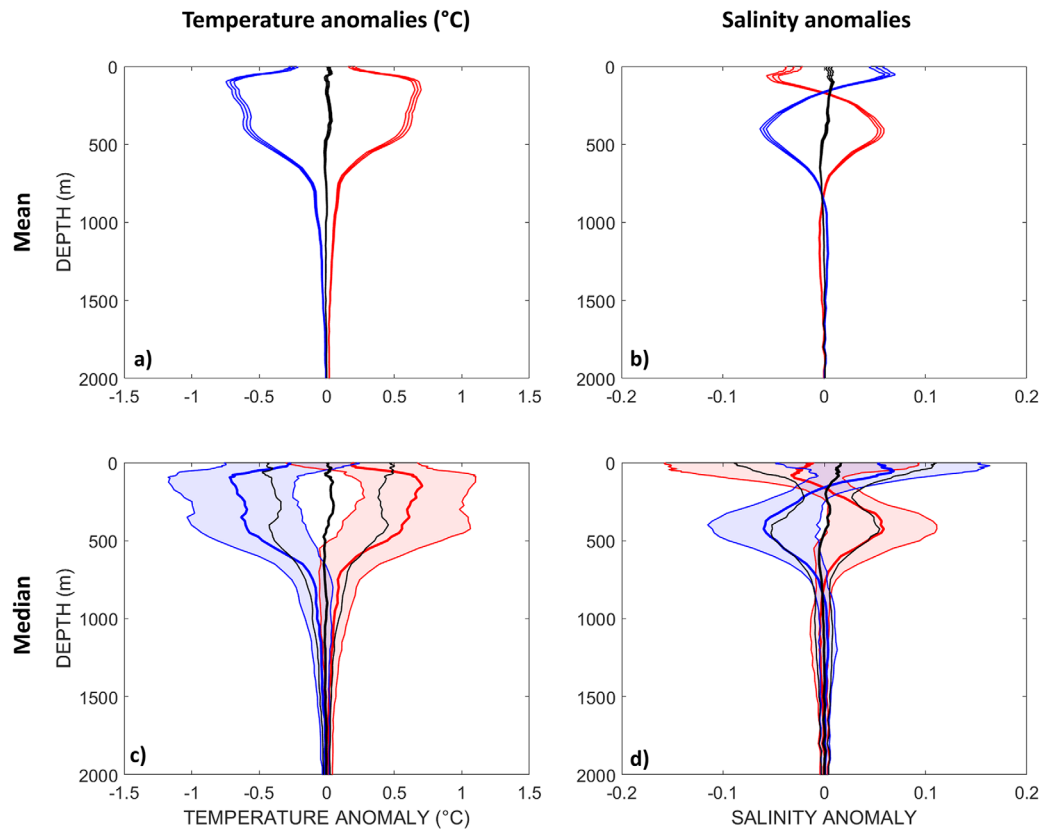


**Figure 7.** Vertical composite structures of temperature and salinity anomalies in subregion S2 (delimited by the blue shape in Figure 1 and 8). Mean anomalies within AE (red), CE (blue) and OE (black) are shown as solid lines for (a, c) temperature and (b, d) salinity. (a, b) Shading shows the standard error above and below the mean or (c, d) between the 25<sup>th</sup> and 75<sup>th</sup> percentile around the median. Note that where the shaded blue and red overlap, it appears purple.

profiles, in particular when surface and subsurface-intensified eddies coexist (e.g., Chaigneau et al., 2011; Pegliasco et al., 2015; Yang et al., 2013).

Eddies in region N2, north of Fiji, were shown to have weaker amplitudes and very weak EKE (see section 3.1). Figures 8 and 9 also reveal that here, the eddies' signatures in temperature and salinity are confined to the upper layer and are smaller than 0.1°C below 500 (600) m for AE (CE). Anticyclonic eddies have a strong signature in sea surface salinity (SSS), with fresh anomalies of about  $-0.1$ . The eddies in region N1 (the Coral Sea Countercurrent), have similar anomaly profiles as in region N2, but they are slightly stronger and deeper. Eddies are thus mostly affecting the upper ocean in and above the thermocline in the northern part of the study region, where the thermocline is close to the surface. The relatively large salinity anomalies near the thermocline in this part of the study region despite the eddies being weaker in these subregions, can be explained by the strongest salinity maximum in the northern part of region at  $\sim 200$  m (Figures 6b–6d).

Contrastingly, eddies in regions S1–S3 extend deeper with anomalies greater than 0.5°C above 500 m, and detectable anomalies ( $> \pm 0.1^\circ\text{C}$ ) at depths greater than 1,000 m. Figures 8 and 9 reveal that vertical profiles in these three subregions exhibit anomalies up to  $\sim 1,000$  m depth. Although the largest temperature and salinity anomalies ( $\pm 1.3$ ,  $\pm 1.0$ ,  $\pm 1.3$  in Figures 9c–9e for temperature and  $\pm 0.10$ ,  $\pm 0.08$ ,  $\pm 0.12$  in Figures 9h–9j for salinity in regions S1–S3 respectively) are found at the depth of the eddy center, temperature and salinity anomalies at the eddy edges are still significant. In these southern regions (S1–S3), where the thermocline is less steep, it would be expected to find smaller eddy-induced temperature and salinity anomalies. However, due to the eddies being more energetic here, they even tend to have a larger effect on the water masses than the northern regions (N1–N2). Whether or not eddies indeed impact water masses at these depths is investigated in the next section.

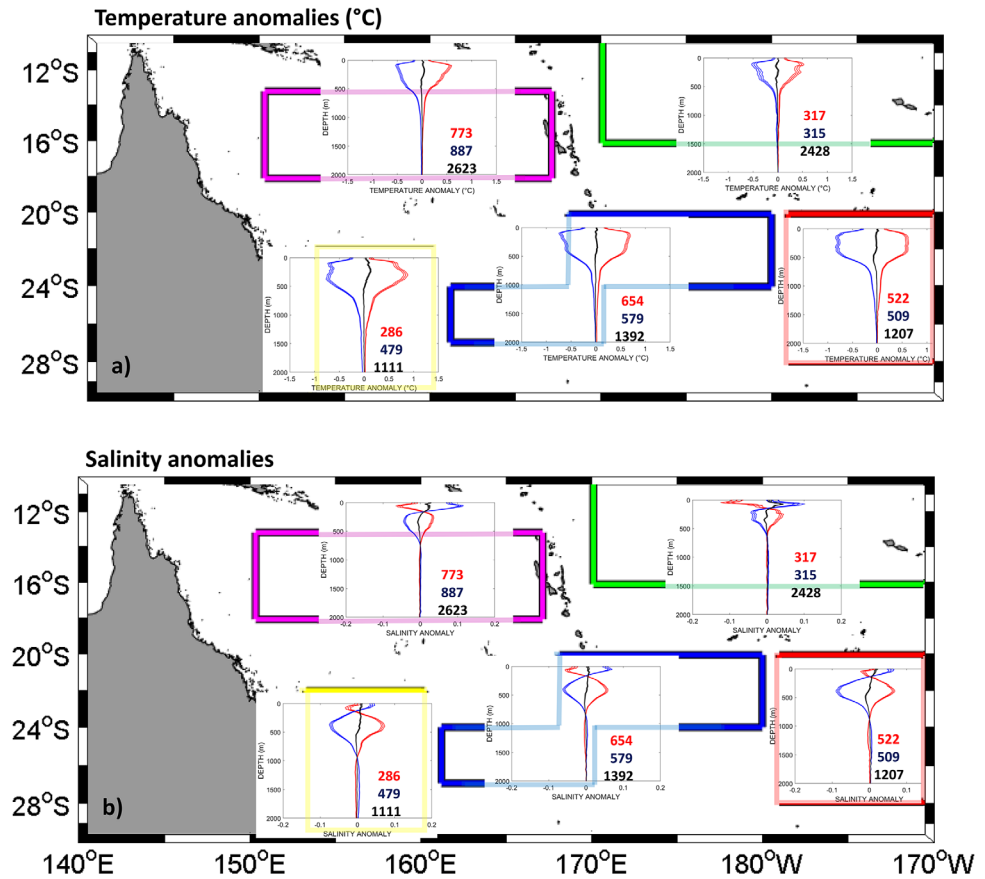


**Figure 8.** Vertical composite structures of temperature and salinity anomalies in the study region. As Figures 7a and 7b for each of the 5 subregions (demarcated with colored shapes in Figure 1). The x and y axes are the same as in Figure 7. The integers indicate the number of floats used to calculate each mean profile in the corresponding colors for AE, CE, and OE.

#### 4.2. Isopycnal Displacements, and Induced T/S Anomalies on Isopycnals

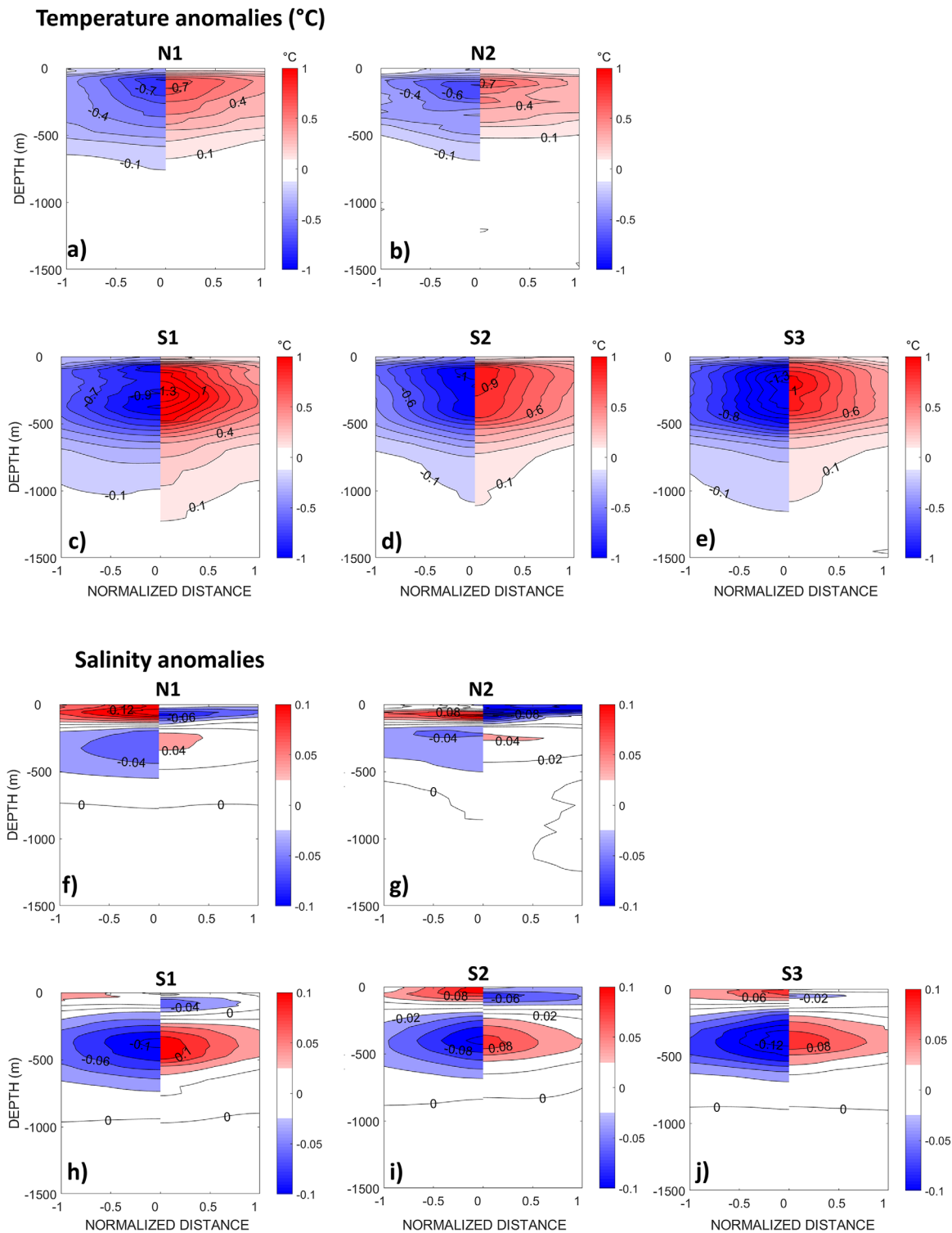
Within eddies, T/S anomalies in the water column can be explained by three main processes: (i) isopycnal vertical displacements due to eddy-induced upwelling or downwelling in the presence of vertical T/S gradients (the largest effect); (ii) diapycnal mixing across isopycnal layers; and (iii) horizontal advection of water properties originating from other regions and trapped inside eddies.

The results shown above (Figures 8 and 9) reveal that eddies impact the water column deeper in the southern regions than in the northern regions. In order to estimate whether this difference can be attributed to the presence of distinct eddy features or only to a change in background vertical stratification between the northern and southern regions, we also computed the mean vertical displacement of isopycnals within eddies (equation (3); Figure 10). For a given vertical isopycnal, isotherm, or isohaline displacement, the resulting anomalies at depth will be larger in more stratified regions. The vertical isopycnal displacement ( $r(z)$ ) was computed for AE and CE separately as follows:

$$r(z) = - \frac{\rho'(z)}{\partial \rho(z) / \partial z} \quad (3)$$

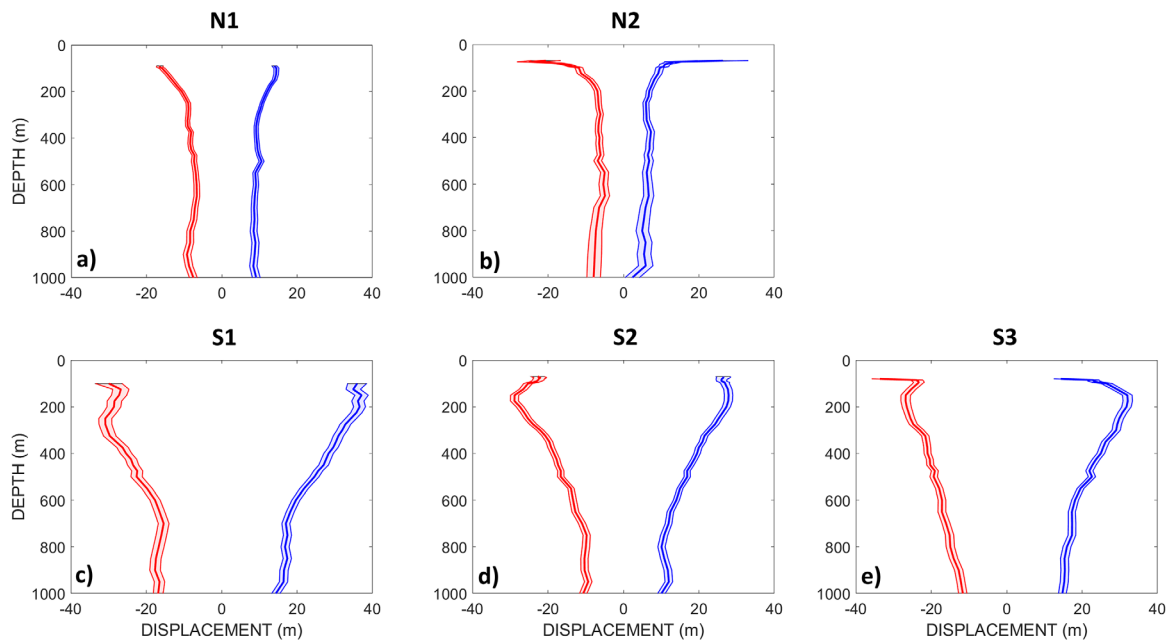
where  $\rho'$  is the density anomaly at each depth (Argo inferred density profile - climatological density), and  $\frac{d\rho}{dz}$  is the local mean vertical density gradient computed from the climatology (Note that the mean displacement outside of eddies was not entirely centered around 0. Hence, this signal was subtracted from the mean displacement in AE and CE to remove an apparent bias in the climatology).

Figure 10 shows that the vertical movement of isopycnals inside eddies has a slightly different behavior in the northern subregions (N1-N2) compared to the southern ones (S1-S3). Eddies in the northern regions



**Figure 9.** 2D vertical composite structures of the (a-e) temperature and (f-j) salinity anomalies as a function of normalized distance from the eddy center for (left) CE and (right) AE in the five subregions from Figure 1 and 8: N1: a, f; N2: b, g; S1: c, h; S2: d, i; S3: e, j. Contour lines are drawn every 0.1°C for temperature and every 0.02 for salinity.

induce an isopycnal displacement of about 15–20 m in the upper 100–150 meters; this displacement is reduced to less than 10 m below 200 m with an almost barotropic effect on the displacement of the isopycnals. The southern regions show greater vertical displacements of the upper layers: depending on the



**Figure 10.** Vertical displacement of isopycnals shown as a function of depth for AE (red) and CE (blue) in the five subregions defined in Figure 1 (a-e correspond to subregions N1-N2, S1-S3). The thick lines show the mean and the shaded regions show the standard error from the mean. The displacements in the mixed layer were removed due to extreme values.

considered subregion, the isopycnals are displaced by  $\sim 30\text{--}40$  m at  $\sim 200$  m, by around  $10\text{--}20$  m at  $\sim 600$  m depth, and to a near-constant value of  $\sim \pm 10\text{--}20$  m below  $\sim 700$  m depth. These results suggest that eddies south of  $\sim 20^\circ\text{S}$  have a stronger subsurface impact, which may not be linked to the differences in the background stratification but instead to inherent eddy properties.

Subsequently, we investigate the cause and effect of the observed T/S anomalies inside eddies: these anomalies could be linked to isopycnal displacement, disappearing after the eddy propagates away, or could reveal a modification of water masses, through trapping and advection of waters from a different region, or local diapycnal mixing. Interestingly, despite a considerably shorter eddy lifetime in the north of the study region (Figure 4c), due to the fast westward propagation there (Figure 4b), the mean traveled distance from the eddy genesis sites to their dissipation sites varies only slightly between  $\sim 250$  and  $\sim 370$  km in each of the subregions (not shown). This indicates that in all five subregions, the mean distance traveled by the eddies is large enough to consider potential water mass transport.

To help differentiate between these processes, and investigate if eddies are indeed trapping water masses of different properties in their core in the different subregions, individual profiles of temperature and salinity anomalies inside eddies are also computed as a function of density instead of depth, and contrasted with temperature and salinity profiles found outside eddies. As temperature and salinity anomalies on isopycnals are inherently compensating each other and are thus identical, only anomalies in salinity are shown (Figure 11). Note that the mean anomalies OE were not zero, and were removed from the composites of anomalies inside AE and CE. The main reason for that is the gridding procedure of the climatological profiles subtracted from the Argo profiles to compute the anomalies. This climatology was obtained from an optimal interpolation on isobaric levels, inducing a smoothing of the salinity extrema compared to averaging performed on isopycnal levels. In addition, some of the profiles considered as being located outside eddies may still be impacted by eddies, as the anomalies detected at the eddy edges are not zero (Figure 9) even if our investigations show that this impact is negligible. Thus, the anomalies inside AE and CE shown in Figure 11 might be slightly underestimated.

The first striking result seen in Figure 11 is that anomalies on isopycnals are very weak; they are of the same order of magnitude as the Argo salinity accuracy of 0.01 (<http://www.argo.ucsd.edu>) and the standard error is often greater than the mean anomaly, preventing us from firm conclusions. Anomalies lower than 0.02 will therefore not be discussed extensively. Some larger signals do however emerge:

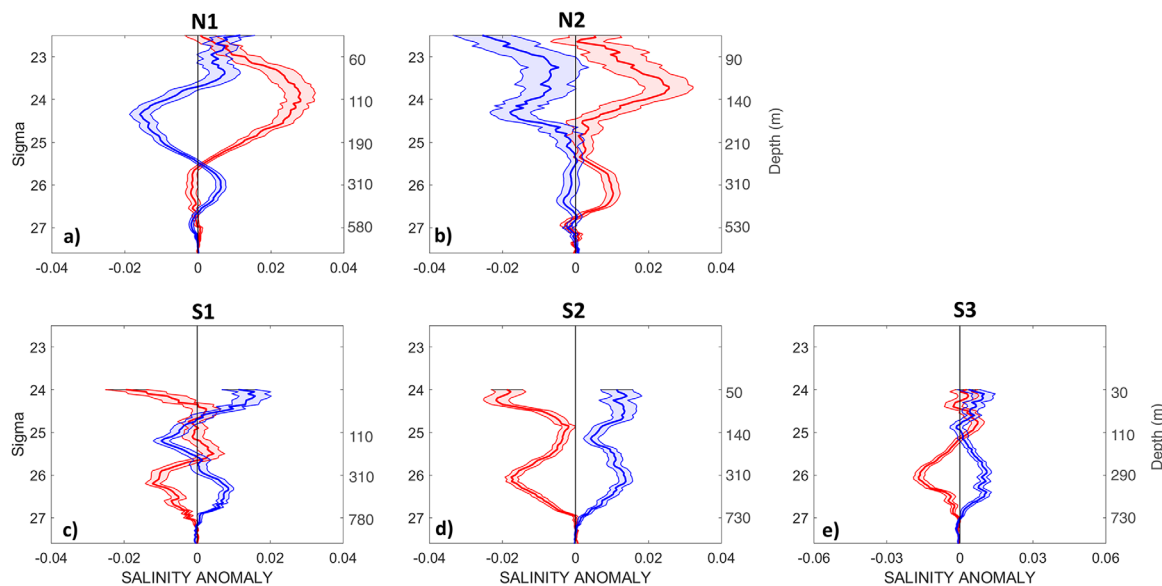


**Figure 11.** Vertical composite structures of the salinity anomalies on isopycnal levels in the five subregions (N1-N2, S1-S3 in Figures 1 and 8). Anomalies within AE (red) and CE (blue) are shown as solid lines. Shading shows the standard error above and below the mean. Note that the mean anomalies OE at each density level were subtracted from the anomalies because it was not centered around zero due to a difference in gridding. Values on shallow density levels, which often outcrop in each subregion, were removed. The approximate equivalent depth of the density levels for each subregion is shown on the secondary y-axes.

1. In subregion N2 North of Fiji, the largest modification is on waters above  $24.5 \text{ kg m}^{-3}$ , on shallow isopycnals above the thermocline. In this region, the mean effect of AE is to induce a warming and salting of the near-surface isopycnal layers, which is not straightforward to interpret. The trapping and transport of warmer and saltier waters on near-surface isopycnals within AE is consistent, given the background horizontal gradients (not shown), with the small poleward propagation of AE observed in the region. However, the impact of CE at these depths is of the opposite sign. It would imply an equatorward propagation of CE, not observed in the region. AE also induce a deepening of the mixed layer of  $7 \pm 25 \text{ m}$ , whereas CE induce a weaker thinning of the mixed layer of  $3 \pm 20 \text{ m}$  (not shown). As such, the anomalies observed within AE, and possibly CE, are also possibly induced by air-sea interactions and diapycnal mixing just below the mixed layer.
2. In subregion N1 in the Coral Sea Countercurrent region, positive salinity anomalies (up to 0.03) are observed inside AE above  $25.5 \text{ kg m}^{-3}$ . As shown in Figure 6, this corresponds to the depths of the SPTW salinity maximum, which erodes along its path westward into the Coral Sea. Such a positive anomaly cannot result from diapycnal mixing with the over and underlying fresher water masses; it thus implies a trapping and an advection of saltier waters from the east and north (see trajectories in Figure 5). This confirms previous assertions that AE in the Coral Sea Countercurrent region may contribute to the mixing of water masses from the saltier NVJ waters to the fresher NCJ waters (Rousselet et al., 2016). The trapping is however mainly restricted to the upper thermocline waters, and does not seem to affect the lower thermocline nor intermediate waters. Anomalies observed inside CE are smaller and of opposite sign, indicating that CE do not appear to trap and transport waters here, but on the contrary may contribute to the erosion of the salinity maximum and to the mixing of upper thermocline water masses in this subregion.
3. In subregion S2 in the STCC, weak negative (positive) salinity anomalies are observed inside AE (CE) between isopycnals  $26\text{--}26.5 \text{ kg m}^{-3}$ , found at around 300–420 m depth (Figure 6). Fresher waters around  $\sigma = 26.2$  inside AE might support the idea of trapped waters being transported westward, given the east-west gradient of properties on this isopycnal. As AE and CE both propagate westward and slightly southward, the observed symmetric behaviors between AE and CE do not advocate for trapping of distinct water masses from the east, but more for diapycnal mixing. The anomalies seen in CE above  $25 \text{ kg m}^{-3}$ , indicate diapycnal mixing in this near-surface area. In the three southern regions (S1-S3), similar anomalies are observed between  $25.5$  and  $27 \text{ kg m}^{-3}$ , the region of the lower thermocline. They are however weak, and do not support the hypothesis of a strong impact on water masses by the eddies.

### 4.3. The Signature of Eddies on Velocity

Geostrophic velocity anomalies relative to a level of no motion at 1,850 m inside eddies are computed from dynamic height anomaly composites (see section 2.2–2.3) (Figure 12). As eddies extend deep and might impact currents below 1,850 m, we tried to infer the eddy absolute geostrophic velocity anomalies by referencing the relative geostrophic velocities to SLA derived surface geostrophic currents. It was found that the errors based on the fact that there may be velocity anomalies at the assumed level of no motion, affect the trapping depth in the northern regions slightly (Figures A3a–A3c) and in the southern regions considerably (Figures A3b–A3d; Table A1), leading to unrealistic results. This method, its validity, and the associated errors are discussed in the Appendix A. The depth at which an eddy's maximum rotational speed  $U$  is greater than its propagation speed  $c$  is also indicated in Figure 12. As discussed by Flierl (1981), Chelton et al. (2011) and many others, the ratio  $U/c$  is a measure of the eddy non-linearity, and a ratio higher than 1 should imply that the eddy traps fluid along its trajectory as it propagates. The contour of the translation speed of the eddies in each subregion thus supposedly highlights how deep water is being trapped by the eddies.

Figure 12 shows that the fastest swirl velocity is found at the surface at approximately halfway between the composite eddy center and its edge. In the region of the EAC, the maximum swirl velocities are  $\sim 25 \text{ cm s}^{-1}$  and  $21 \text{ cm s}^{-1}$  in AE and CE respectively. In this region, where eddies tend to have the strongest EKE and largest amplitude (Figures 3c and 3d), the mean trapping depth is the deepest in the study region with approximately 800 m and velocity anomalies of more than  $-1 \text{ cm s}^{-1}$  are still detected at depths greater than 1,500 m in CE. In the region south and east of New Caledonia (subregion S2, Figure 12d), the eddy maximum velocity anomalies are 23 (25)  $\text{cm s}^{-1}$  in AE (CE) and the eddy trapping depth is  $\sim 400$  m. Eddies impact the velocities down to  $\sim 1,300$  m, with a mean weak anomaly of  $\pm 1 \text{ cm s}^{-1}$ . The south-eastern area of the study region (subregion S3, Figure 12e) displays a similar composite structure, with eddy maximum velocity anomalies reaching 17 (15)  $\text{cm s}^{-1}$  in AE (CE), effectively trapping water to  $\sim 400$  m.

In the tropics, the trapping depth is much shallower. In the CSCC (subregion N1, Figure 12a), the eddy maximum velocity anomalies reach 19 (17)  $\text{cm s}^{-1}$  respectively, trapping waters only above  $\sim 200$  m. In region N2 (Figure 12b), maximum velocity anomalies reach 5 (17)  $\text{cm s}^{-1}$  in AE (CE); eddies in this region also

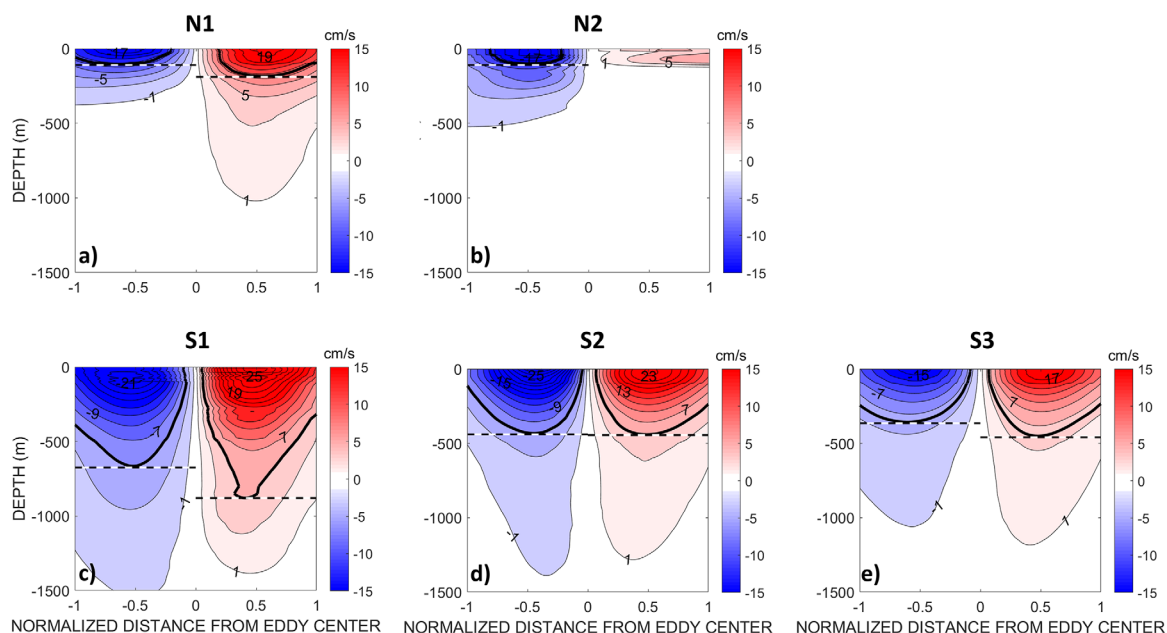


**Figure 12.** Composite geostrophic velocity (derived from the dynamic height) as a function of depth and normalized distance from the eddy center in the 5 subregions (N1–N2, S1–S3) for CE (blue shading) and AE (red shading). Contour lines are drawn every  $2 \text{ cm s}^{-1}$ . The thick black line shows the contour where the geostrophic velocity equals the mean propagation velocity in the subregions (10, 12, 5, and  $4 \text{ cm s}^{-1}$  in the subregions N1–N2, S1–S3 respectively). The dashed lines show the respective trapping depth.

propagate faster. As a result, composite AE are not able to trap and transport waters, whereas composite CE may only be able to trap near-surface surface waters above  $\sim 100$  m.

## 5. Discussion and Conclusions

The objectives of this study were to describe the main characteristics of mesoscale eddies in the Southwest Tropical Pacific Ocean (SWTP): to investigate their generation, propagation, and their surface properties; to examine their vertical extent in terms of temperature, salinity, and velocity, and to evaluate how deep they affect the mean currents and the physical properties in the water column. The ultimate goal was to investigate the contribution of these coherent structures to the transport of water masses in this region of transit from the subtropics to the equatorial band and high latitudes, and their contribution to the mixing of water masses. In order to provide some answers to these questions, we took advantage of the complementarity of two widely used data sets: Sea Level Anomaly (SLA) data from satellite altimetry allowing detection of surface mesoscale eddies, together with vertical temperature and salinity profiles from Argo floats surfacing into eddies.

Our region of interest encompasses tropical and extra-tropical latitudes, areas of energetic and weaker currents, with vertical and horizontal shears, and numerous islands influencing the propagation of eddies. Therefore, the region was divided into five subregions corresponding to contrasting EKE or water pathways, in which different eddy properties were expected. Table 4 summarizes some of the main eddy properties in these subregions.

Our findings indicate that north of the Fiji archipelago (region N2), in the tropical area of the Southwest Pacific, eddies are rather sparse. They tend to have large radii, weak amplitudes, do not live more than a few weeks, and only impact the upper ocean above  $\sim 200$  m, through downward (upward) pumping inside AE (CE), and isopycnal displacements of approximately 15 meters. Their typical signature on temperature, salinity, and velocities are weak ( $\pm 0.6^\circ\text{C}$ ,  $\pm 0.1$ , and  $10 \text{ cm s}^{-1}$ , respectively); they do not appear to be able to trap and transport waters, but AE seem to contribute to the mixing of these upper waters, in and below the mixed layer. This is consistent with the recent investigations of eddy properties inside the nearby Solomon Sea (Gourdeau et al., 2017). It is also consistent with previous conclusions, highlighting that at these latitudes, equatorward of  $20^\circ$ , most of the propagating energy is in the form of linear Rossby waves, not of nonlinear eddies.

West of Vanuatu (region N1) is where two westward currents, which are transporting water masses from different origin into the Coral Sea, the NVJ and NCJ, experience lateral shear with the eastward Coral Sea Countercurrent flowing between them. In this subregion, where high EKE has been suggested to result from barotropic instability due to this shear between adjacent opposite mean currents (Qiu et al., 2009), our results show that mesoscale eddies are indeed numerous; most of them were generated in the lee of Vanuatu, and gain EKE when propagating westward. They tend to have higher amplitudes than in the same latitude range east of Vanuatu, and have a signature in temperature and salinity higher than  $0.3^\circ\text{C}$  and  $0.02$ , respectively, down to  $\sim 500$  m depth. Rousselet et al. (2016) suggested that AE participate in the transport and mixing of water masses from the NVJ to the NCJ in this Coral Sea Countercurrent region. In agreement with this study, we find that AE in the Coral Sea countercurrent region are indeed able to trap waters above  $200$  m, to transport salty SPTW waters from the NVJ to the NCJ above  $\sigma = 25 \text{ kg m}^{-3}$ , and to contribute to

**Table 4**  
Summary of Mean Eddy Properties in the Subregions (AE and CE Combined)

Subregion	Radius (km)	Amplitude (cm)	EKE ( $\text{cm}^2/\text{s}^2$ )	Lifetime (weeks)	Propagation velocity (cm/s)	Max. swirl velocity (cm/s)	Approx. trapping depth (m)
N1	110	6	193	10	10	19	200
N2	141	4	101	5	12	17	100
S1	95	12	382	21	5	25	800
S2	105	9	195	24	5	25	400
S3	108	8	174	27	4	17	400

the mixing of these two water masses. Interestingly, CE do appear to have a different impact, and to contribute weakly to the salinity maximum erosion. This is the only region in the Southwest Pacific where our study shows evidence of water mass trapping inside eddies.

South and southeast of New Caledonia, along the path of the STCC region (regions S2-S3), eddies tend to have larger amplitudes ( $\sim 9$  cm), smaller radii ( $\sim 100$  km), and larger EKE ( $\sim 200$   $\text{cm}^2 \text{s}^{-2}$ ), and much longer lifetimes ( $\sim 26$  weeks). As such, they are ubiquitous in these regions and can be observed with a frequency of  $\sim 200,000$  in the 22-year period between 1993 and 2014. Region S2 is an area of high EKE that has been suggested to result from baroclinic instabilities of the sheared STCC-SEC current system (Qiu & Chen, 2004). Our study reveals that eddies have on average a deeper effect on the seawater properties than toward the north of the study region, with composite anomalies of  $\pm 0.1^\circ\text{C}$ , and  $1$   $\text{cm s}^{-1}$  down to  $\sim 1,000$  m depth. The displacement of the isopycnals is also considerably larger in the south, indicating that the differences in vertical temperature anomalies are not just an effect of similar displacements on a different background stratification. This is consistent with the theory, indicating that in this region south of  $20^\circ\text{S}$ , both effects of weaker stratification (Figure 6) and higher Coriolis parameter compared to the region north of  $20^\circ\text{S}$  lead to a larger vertical extent (see Zhang et al., 2013). The trapping depth is found to be around 400 m or deeper, signifying that upper and lower thermocline waters are not only pumped down (up) inside AE (CE) but might also be trapped and transported along eddies trajectories. However, in these southern regions, when looking for salinity and temperature anomalies on sigma levels, our methodology did not find any indication that water masses are indeed trapped and transported inside eddies. Our results on the contrary suggest that eddies contribute to the mixing of SEC lower thermocline waters advected westward below the surface eastward flowing STCC. Our findings also suggest that eddies do not impact deeper intermediate waters, and do not play a significant role in the erosion of their salinity properties observed during their transit in the region.

The deepest eddies are found in the region of the EAC (region S1), a western boundary current characterized by a very energetic eddy field. Eddies there have a mean amplitude of  $\sim 12$  cm, and a mean EKE of  $\sim 400$   $\text{cm}^2 \text{s}^{-2}$ , which is significantly higher than in the rest of the SWTP (Table 4). Eddies in the EAC have been extensively studied southward of  $30^\circ\text{S}$ , where the EAC is well developed and separates from the coast, and have been suggested to contribute significantly to the southward transport of the Coral Sea waters (e.g., Everett et al., 2012). Our results reveal that eddies are associated with upward or downward isopycnal displacements of around  $\sim 30$  m down to 500 m, resulting in temperature anomalies up to  $\pm 0.8^\circ\text{C}$ , and velocity anomalies greater than  $7$   $\text{cm s}^{-1}$  down to this depth. Although they should be able to trap waters to 800 m depth, the dispersion of the anomalies on isopycnals within eddies is such that composites are not meaningful, and our method could not confirm the presence of different water masses trapped and transported inside these nonlinear eddies.

As the Rossby radius of deformation and the stratification vary with latitude, differences in eddy properties and structures occur at different latitudes. Given this diversity of eddy structures, and the absence of evidence of water mass trapping inside them, attempting to compute a mean heat and salt transport based on the number of eddies and their trapping depth in the region did not appear meaningful.

Our work, providing vertical eddy composites in the region, will also be useful for at least two applications: it will help to deconvolute the effect of an eddy on a vertical cruise profile or synoptic glider section and will allow the estimation of transport anomalies associated with a transient eddy. Attempts have been made in the region to estimate transport variability from altimetric fields at seasonal to interannual timescales, assuming that the transport variability at these timescales is surface-intensified and well correlated with satellite-derived surface geostrophic currents (Kessler & Cravatte, 2013a; Melet et al., 2010; Ridgway et al., 1993). Kessler and Cravatte (2013a) proposed a simple index of the transport variability entering into the Coral Sea between the Solomon Islands and New Caledonia, based on the surface current anomaly multiplied by an equivalent depth of 158 m for the 0–1,000 m transport. Without knowing the eddy depth scale, they were unable to estimate the transport anomaly at intraseasonal timescales associated with the propagation of mesoscale eddies. Our results here suggest that eddies north of New Caledonia are mostly shallow, but that their impact on transport variability cannot be estimated simply from surface velocity anomalies, their mean equivalent depth varying from 130 to 300 m. However, they do contribute to an instantaneous transport anomaly of around 4 Sv in the 0–1,000 m layer, as computed from the composites. South of New Caledonia, the typical equivalent depth is around 300–350 m, much larger than the one

estimated for interannual variability. Eddies can alias the transports by around 8 to 12 Sv in the 0–1,000 m layer, which is significant and of the same order of magnitude as the mean currents. These results provide a tool to use satellite altimetry in synergy with synoptic transects to estimate roughly the aliasing in transport due to the occurrence of mesoscale eddies. They also underline the importance of using a time sampling strategy to be able to use sparse repeated synoptic sections to estimate interannual transport variability.

While our study described the characteristics of the mesoscale eddies in the Southwest Pacific both at the surface and vertically, it gives rise to new questions. One of the objectives was to document the eddy generation, behavior, and decay in this region of particularly complex topographic obstacles and instabilities. Our study suggests that eddies appear to be impacted by the topography, with fewer eddies above ridges and shallow bathymetry. Our study also reveals that nearly half of the detected eddies decay when encountering the eastern coast of an island, whereas much of the eddies in the region are generated in the lee of the islands. Exploring the possible mechanisms of dissipation east of the islands, and of generation west of the islands are beyond the scope of this study, but should be investigated in a following study. Instabilities of the sheared currents found west of the islands (Cravatte et al., 2015) are one of the possible mechanisms. Alternatively, southeasterly trade winds prevailing in the region are modified by the presence of high mountains in Fiji, Vanuatu, and New Caledonia. This obstruction creates wind stress curl dipoles in the lee of the islands (Qiu et al., 2009), very similar to those observed in the lee of the Hawaiian Islands (Yoshida et al., 2010). Such wind stress curls possibly generate eddies west of the islands. The last possibility is that our tracking method, applied on an imperfect gridded SLA product based on interpolated altimetric tracks, lost eddies and identified erroneously newly generated eddies in the vicinity of islands. We therefore suggest that a similar study should be performed applying the same eddy tracking algorithm in high-resolution numerically modeled SLA fields resolving the islands topography.

One unanticipated conclusion is the high variability of eddy structures obtained with our methodology. Even with several hundreds of vertical profiles sampling AE and CE properties, vertical temperature and salinity anomalies inside eddies are scattered around the mean composite. Whether such dispersions are linked to the diversity of eddy vertical structures, to errors in the interpolated altimetric fields, in the detection method, or to other sources of variability such as interannual variability or internal waves is not known and could also be investigated using oceanic model simulations.

Finally, the temporal variability of the eddy occurrence, and more specifically, the interannual variability of eddy structures can be further investigated in this region influenced by ENSO (El Niño Southern Oscillation). Their role for the mixing could be modulated at interannual timescales. Supplementary observational data sets could be used to investigate the vertical structure of eddies near the coasts and their behavior around islands. The impact of eddies on primary production could be analyzed by colocalizing the detected eddies with satellite maps of ocean color; and their impact on coastal areas and their ability to trap and transport coastal waters to the open ocean should be investigated.

## Appendix A: Methods for Estimating Mean Absolute and Relative Geostrophic Velocity Anomalies Inside Eddies, and Associated Errors

To subsequently derive geostrophic velocities, the dynamic height anomaly composite computed from irregularly sampled Argo profiles inside eddies must be mapped with great care. Indeed, a small change in the radial slope leads to significant differences in resulting geostrophic velocities. In this appendix, an estimate of the errors associated with the relative geostrophic velocity is provided. A method to estimate the absolute geostrophic velocity is also presented and discussed. The northern (N1-N2) and southern (S1-S3) regions are combined because the velocity estimates based on too few observations lead to much larger errors.

### A1. Estimation of the Absolute Geostrophic Velocity Anomalies at the Surface

The composite SLA (black dashed lines in Figures A1a and A1b) is obtained by averaging all SLA anomalies within the AE and CE contours and hence includes much more data than when comparing SLA or dynamic height only at the position of the Argo floats. The absolute surface geostrophic velocity anomalies can then be computed based on this composite SLA with high accuracy (black dashed lines in Figures A1c and A1d).

**Table A1**  
Errors Between the Different Methods to Estimate the Geostrophic Velocity

Regions	SLA Gauss/ SLA composite AE	SLA Gauss/ SLA composite CE	SLA Gauss/ DH Gauss AE	SLA Gauss/ DH Gauss CE	SLA composite/ DH Gauss AE	SLA composite/ DH Gauss CE
N1-N2	25%	29%	41%	52%	55%	72%
S1-S3	31%	23%	45%	16%	41%	42%

Note. (left to right): Errors between the SLA at the Argo position with a Gaussian Fit and the composite SLA for AE and CE; between the SLA at the Argo position with a Gaussian fit and the dynamic height (DH) at the surface with a Gaussian Fit; total error between the composite SLA and the DH at the surface with a Gaussian fit.

### A2. Gaussian Fit to Irregularly Sampled Argo Profiles

To estimate the error associated with the geostrophic velocity due to the mapping of irregular Argo float dynamic height anomalies, daily altimetric SLA fields are first subsampled at the position of the Argo floats surfacing inside AE and CE. A Gaussian fit is then applied to these irregular SLA observations (blue and red lines in Figures A1a and A1b). The result is compared to the SLA composites (black dashed lines in Figures A1a and A1b). Geostrophic velocity anomalies are then derived from the radial gradient of both SLA composites and are shown in Figures A1c and A1d in the corresponding colors.

The difference between the methods is shown in Figure A2 (red and blue solid lines), highlighting the error simply due to the sampling and fitting methods: in the northern regions (N1-N2, Figure A2a), the error in AE increases from the center to the eddy edge with over  $\pm 10 \text{ cm s}^{-1}$  at the edge. In the same regions, the error in CE is does not exceed  $\pm 4 \text{ cm s}^{-1}$ . In the southern regions (S1-S3, Figure A2b), the error in AE is up to

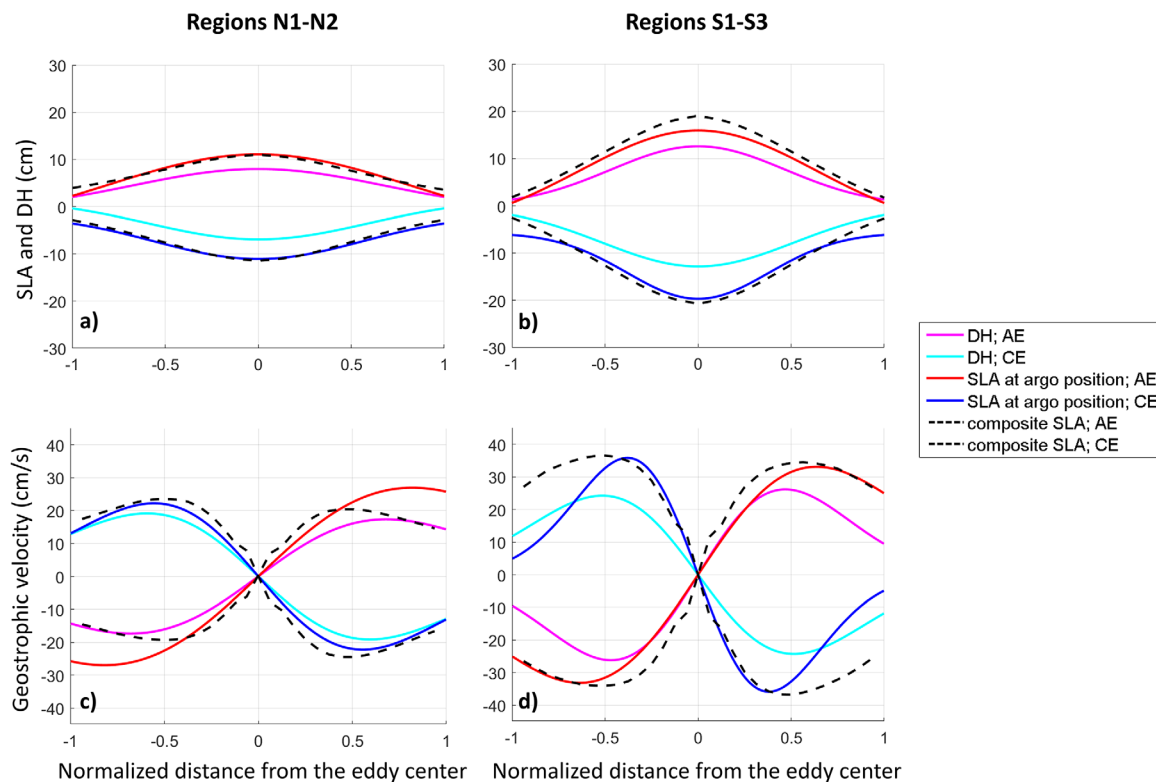


**Figure A1.** Comparison of methods. (a, b) SLA composite and at the Argo floats' position, and dynamic height (DH); (c, d) corresponding geostrophic velocity at the surface in the subregions (combined for the regions N1-N2 (a, c) and for the regions S1-S3 (b, d)). AE are in red and magenta; CE are in blue and cyan. The composite SLA is in black dashed lines, the SLA only at the Argo positions in red and blue solid lines, and the DH at the surface is in magenta and cyan solid lines. Note that for (a, b), the mean SLA for the study period (5.7 cm) was subtracted from the SLA for easier comparison with the DH.

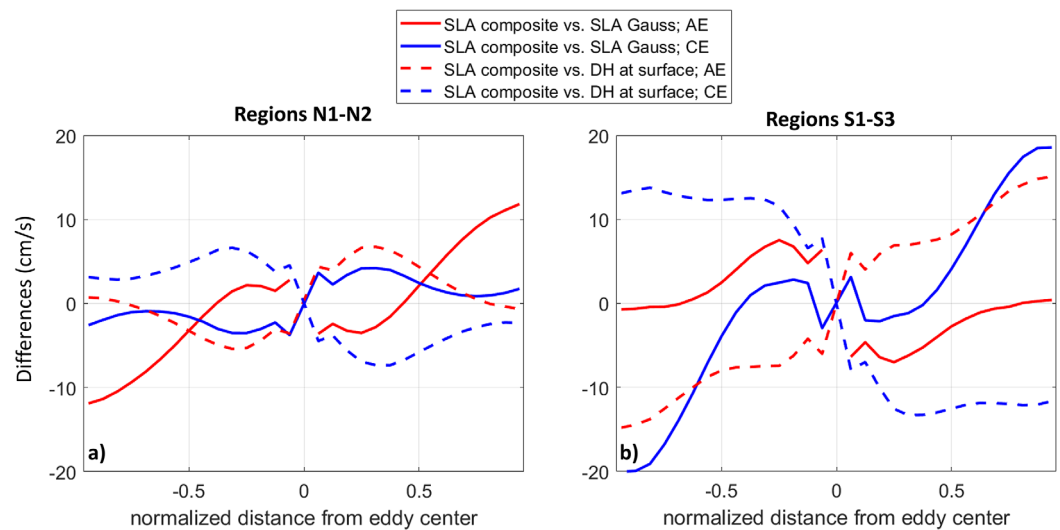


**Figure A2.** Differences between the geostrophic velocities based on different methods in the subregions (combined for (a) N1-N2 and (b) for S1-S3). The SLA composite minus the Gaussian fit of the SLA is in red (AE) and blue (CE) solid lines; the SLA composite minus the Gaussian fit of the dynamic height (DH) at the surface is in red (AE) and blue (CE) dashed lines.

$\pm 7 \text{ cm s}^{-1}$ , which is largest at  $\sim \frac{1}{3}$  of the distance from the center to the edge and smallest near the center and at  $\sim \frac{2}{3}$  of the radius. In the same region, the error in CE is largest at the edge with up to  $\pm 20 \text{ cm s}^{-1}$ .

### A3. Estimation of the Relative Geostrophic Velocity Anomalies

As explained in section 2.3, a Gaussian fit is applied to map the dynamic height anomaly profiles relative to the 1,850 m reference level inside AE and CE. The error that is present due to the difference in the observations of the dynamic height at the surface and the SLA is shown in Figure A2. This error is explained by a possible non-zero velocity anomaly at the assumed level of no motion (1,850 m). In the southern regions (S1-S3, Figure A2b), the differences in geostrophic surface velocity anomaly derived from SLA composites and from dynamic height anomalies (red and blue dashed lines in Figure A2). In the northern regions (N1-N2, Figure A2a), this error is up to  $\pm 5$  (7)  $\text{cm s}^{-1}$  in AE (CE) and in the southern regions, this error is up to  $\pm 14$  (11)  $\text{cm s}^{-1}$  in AE (CE),

### A4. Summary of Errors

The error between the different approaches of computing the geostrophic velocity is shown in Table A1. It illustrates that the error, which is expected to be mainly due to the methods (the error between the composite SLA and the Gaussian fit to the SLA at the Argo float positions), is between 23% and 31%. The error mainly thought to be due to assuming a level of no motion (the error between the Gaussian fit of the SLA at the Argo position and the same method for the dynamic height at the surface), is between 16% and 52%. This results in a total error (between the composite SLA and the Gaussian fit of the dynamic height at the surface) between 41% and 72%. In our analysis, we found that these errors tend to decrease when choosing more uniform regions, and when using areas that contain many floats.

### A5. Absolute Geostrophic Velocity at Depth (Based on the SLA-Fitted Dynamic Height)

The dynamic height composite is less steep than the SLA composite, resulting in slower relative swirl velocities. As mentioned in the previous sections, we assume that the difference in velocity from these two estimations (SLA and dynamic height) can be considered as an estimation of the neglected velocity anomaly at 1,850 m. Adding this difference to the relative geostrophic velocity anomalies on the whole depth thus gives estimates of the absolute geostrophic velocity anomalies inside eddies. When comparing the relative geostrophic velocity (Figures A3a and A3b) with the absolute geostrophic velocity (Figures A3c and A3d), the maximum velocities at the surface increases slightly in intensity. In the northern regions (N1-N2), the trapping depths of the adjusted velocity (Figure A3c) increase to  $\sim 200 \text{ m}$  from  $\sim 100 \text{ m}$  when using the relative velocity (Figure A3a). However, in the southern regions (S1-S3), as the velocity increases at the eddy edges in the

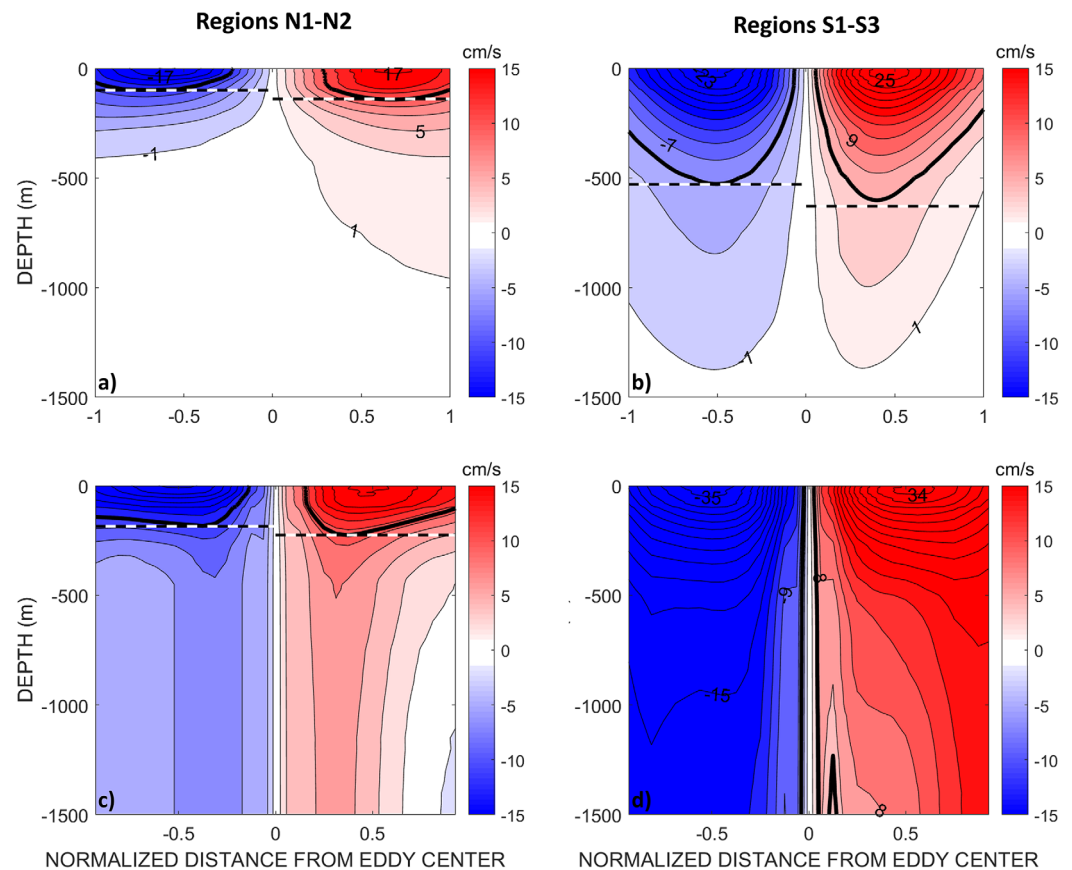


**Figure A3.** Composite geostrophic velocity with and without offset. (a, b) Same as Figure 12, (a, c) but for subregions N1-N2 combined, and (b, d) for subregions S1-S3. The top panel is without offset from the SLA. In the bottom panel, the difference between the composite SLA and the dynamic height at the surface was added to the dynamic height at all depth levels before the velocity was computed.

#### Acknowledgments

The authors wish to acknowledge Ssalto/Duacs AVISO who produced the altimeter products, with support from CNES (<http://www.aviso.altimetry.fr/duacs/>). This study has also been possible thanks to the amount of Argo data, collected and made freely available by the International Argo Program and the national programs that contribute to it. The Argo Program is part of the Global Ocean Observing System (DOI <http://doi.org/10.17882/42182>). The authors also thank the Scripps Institute for Oceanography for making available their gridded Argo product. This work benefited from discussions with C. Menkes, F. Marin, F. Durand, and Y. Morel and from input by P. Landschützer. L. Keppler was funded by USP, IRD and the MPI-M. S. Cravatte, A. Chaigneau, and L. Gourdeau are funded by IRD. A. Singh is funded by USP. This work is a contribution to the joint CNES/NASA OSTST project "Merging of satellite and in situ observations for the analysis of meso and submesoscale dynamics", to the NASA/CNES SWOT-ST project "SWOT in the tropics", and to the CLIVAR/SPICE International program. This work is co-funded by INSU/LEFE and CNES.

whole water column, the adjusted velocity (Figure A3d) shows considerably deeper trapping depths of  $>1,500$  m in both AE and CE, compared to  $\sim 500$  m of relative velocity (Figure A3b). This seems very unlikely.

Due to the mentioned errors and uncertainties between the methods, it would be useful to colocalize in situ velocity observations with eddies and compare the findings with our results.

#### References

- Amores, A., Melnichenko, O., & Maximenko, N. (2017). Coherent mesoscale eddies in the North Atlantic subtropical gyre: 3-D structure and transport with application to the salinity maximum. *Journal of Geophysical Research: Oceans*, *122*, 23–41. <https://doi.org/10.1002/2016JC012256>
- Argo. (2000). Argo float data and metadata from Global Data Assembly Centre (Argo GDAC). SEANOE. Retrieved from <http://www.seanoe.org/data/00311/42182/>; <https://doi.org/10.17882/42182>
- Barnes, S. L. (1973). *Mesoscale objective map analysis using weighted time-series observations* (NOAA Tech. Memo. ERL NSSL-69, 60 pp.). Norman, OK: National Severe Storm Laboratory.
- Bowen, M. M., Wilkin, J. L., & Emery, W. J. (2005). Variability and forcing of the East Australian Current. *Journal of Geophysical Research*, *110*, C03019. <https://doi.org/10.1029/2004JC002533>
- Brassington, G. B., Summons, N., & Lumpkin, R. (2011). Observed and simulated Lagrangian and eddy characteristics of the East Australian Current and the Tasman Sea. *Deep Sea Research Part II: Topical Studies in Oceanography*, *58*(5), 559–573. <https://doi.org/10.1016/j.dsr2.2010.10.001>
- Cai, W. (2006). Antarctic ozone depletion causes an intensification of the Southern Ocean super-gyre circulation. *Geophysical Research Letters*, *33*, L03712. <https://doi.org/10.1029/2005GL024911>
- Castelao, R. M. (2014). Mesoscale eddies in the South Atlantic Bight and the Gulf Stream Recirculation region: Vertical structure. *Journal of Geophysical Research: Oceans*, *119*, 2048–2065. <https://doi.org/10.1002/2014JC009796>
- Ceccarelli, D. M., McKinnon, A. D., Andrefouet, S., Allain, V., Young, J., Gledhill, D. C., et al. (2013). The coral sea: Physical environment, ecosystem status and biodiversity assets. In M. Lesser (Ed.), *Advances in marine biology* (Vol. 66, pp. 213–290). San Diego, CA: Elsevier Academic Press Inc.

- Chaigneau, A., Eldin, G., & Dewitte, B. (2009). Eddy activity in the four major upwelling systems from satellite altimetry (1992–2007). *Progress in Oceanography*, 53(1–4), 117–123. <https://doi.org/10.1016/j.pocean.2009.07.012>
- Chaigneau, A., Gizolme, A., & Grados, C. (2008). Mesoscale eddies off Peru in altimeter records: Identification algorithms and eddy spatio-temporal patterns. *Progress in Oceanography*, 59(2–4), 106–119. <https://doi.org/10.1016/j.pocean.2008.10.013>
- Chaigneau, A., Le Texier, M., Eldin, G., Grados, C., & Pizarro, O. (2011). Vertical structure of mesoscale eddies in the eastern South Pacific Ocean: A composite analysis from altimetry and Argo profiling floats. *Journal of Geophysical Research*, 116, C11025. <https://doi.org/10.1029/2011JC007134>
- Chelton, D. B., Schlax, M. G., & Samelson, R. M. (2011). Global observations of nonlinear mesoscale eddies. *Progress in Oceanography*, 59(2), 167–216. <https://doi.org/10.1016/j.pocean.2011.01.002>
- Couvelard, X., Marchesiello, P., Gourdeau, L., & Lefèvre, J. (2008). Barotropic zonal jets induced by islands in the southwest Pacific. *Journal of Physical Oceanography*, 38(10), 2185–2204. <https://doi.org/10.1175/2008JPO3903.1>
- Cravatte, S., Ganachaud, A., Duong, Q.-P., Kessler, W. S., Eldin, G., & Dutrieux, P. (2011). Observed circulation in the Solomon Sea from SADC data. *Progress in Oceanography*, 58(1–4), 116–130. <https://doi.org/10.1016/j.pocean.2010.12.015>
- Cravatte, S., Kestenare, E., Eldin, G., Ganachaud, A., Lefèvre, J., Marin, F., et al. (2015). Regional circulation around New Caledonia from two decades of observations. *Journal of Marine Systems*, 148, 249–271. <https://doi.org/10.1016/j.jmarsys.2015.03.004>
- Davis, R. E., Kessler, W. S., & Sherman, J. T. (2012). Gliders Measure Western Boundary Current Transport from the South Pacific to the Equator\*. *Journal of Physical Oceanography*, 42(11), 2001–2013. <https://doi.org/10.1175/JPO-D-12-022.1>
- Dong, C., McWilliams, J. C., Liu, Y., & Chen, D. (2014). Global heat and salt transports by eddy movement. *Nature Communications*, 5, 3294. <https://doi.org/10.1038/ncomms4294>
- Everett, J. D., Baird, M. E., Oke, P. R., & Suthers, I. M. (2012). An avenue of eddies: Quantifying the biophysical properties of mesoscale eddies in the Tasman Sea. *Geophysical Research Letters*, 39, L16608. <https://doi.org/10.1029/2012GL053091>
- Fine, R. A., Lukas, R., Bingham, F. M., Warner, M. J., & Gammon, R. H. (1994). The western equatorial Pacific: A water mass crossroads. *Journal of Geophysical Research*, 99(C12), 25063–25080. <https://doi.org/10.1029/94JC02277>
- Flierl, G. R. (1981). Particle motions in large-amplitude wave fields. *Geophysical & Astrophysical Fluid Dynamics*, 18(1–2), 39–74. <https://doi.org/10.1080/03091928108208773>
- Frenger, I., Muennich, M., Gruber, N., & Knutti, R. (2015). Southern Ocean eddy phenomenology. *Journal of Geophysical Research: Oceans*, 120, 7413–7449. <https://doi.org/10.1002/2015JC011047>
- Ganachaud, A., Cravatte, S., Melet, A., Schiller, A., Holbrook, N. J., Sloyan, B. M., et al. (2014). The Southwest Pacific Ocean circulation and climate experiment (SPICE). *Journal of Geophysical Research: Oceans*, 119, 7660–7686. <https://doi.org/10.1002/2013JC009678>
- Ganachaud, A., Gourdeau, L., & Kessler, W. (2008). Bifurcation of the Subtropical South Equatorial Current against New Caledonia in December 2004 from a hydrographic inverse box model. *Journal of Physical Oceanography*, 38(9), 2072–2084. <https://doi.org/10.1175/2008JPO3901.1>
- Gasparin, F., Ganachaud, A., Maes, C., Marin, F., & Eldin, G. (2012). Oceanic transports through the Solomon Sea: The bend of the New Guinea Coastal Undercurrent. *Geophysical Research Letters*, 39, L15608. <https://doi.org/10.1029/2012GL052575>
- Gasparin, F., Maes, C., Sudre, J., Garçon, V., & Ganachaud, A. (2014). Water mass analysis of the coral sea through an optimum multiparameter method. *Journal of Geophysical Research: Oceans*, 119, 7229–7244. <https://doi.org/10.1002/2014JC010246>
- Germineaud, C., Ganachaud, A., Sprintall, J., Cravatte, S., Eldin, G., Alberty, M. S., & Privat, E. (2016). Pathways and Water Mass Properties of the Thermocline and Intermediate Waters in the Solomon Sea. *Journal of Physical Oceanography*, 46(10), 3031–3049. <https://doi.org/10.1175/JPO-D-16-0107.1>
- Gourdeau, L., Kessler, W. S., Davis, R. E., Sherman, J., Maes, C., & Kestenare, E. (2008). Zonal Jets Entering the Coral Sea. *Journal of Physical Oceanography*, 38(3), 715–725. <https://doi.org/10.1175/2007JPO3780.1>
- Gourdeau, L., Veiron, J., Chaigneau, A., Cravatte, S., & Kessler, W. (2017). Complementary use of glider data, altimetry, and model for exploring meso scale eddies in the tropical Pacific Solomon Sea. *Journal of Geophysical Research: Oceans*, 122, 9209–9229. <https://doi.org/10.1002/2017JC013116>
- Grenier, M., Cravatte, S., Blanke, B., Menkes, C., Koch-Larrouy, A., Durand, F., et al. (2011). From the western boundary currents to the Pacific Equatorial Undercurrent: Modeled pathways and water mass evolutions. *Journal of Geophysical Research*, 116, C12044. <https://doi.org/10.1029/2011JC007477>
- Grenier, M., Jeandel, C., & Cravatte, S. (2014). From the subtropics to the equator in the Southwest Pacific: Continental material fluxes quantified using neodymium data along modeled thermocline water pathways. *Journal of Geophysical Research: Oceans*, 119, 3948–3966. <https://doi.org/10.1002/2013JC009670>
- Grenier, M., Jeandel, C., Lacan, F., Vance, D., Venchiarutti, C., Cros, A., & Cravatte, S. (2013). From the subtropics to the central equatorial Pacific Ocean: Neodymium isotopic composition and rare earth element concentration variations. *Journal of Geophysical Research: Oceans*, 118, 592–618. <https://doi.org/10.1029/2012JC008239>
- Holbrook, N. J., Chan, P. S.-L., & Venegas, S. A. (2005). Oscillatory and propagating modes of temperature variability at the 3–3.5- and 4–4.5-yr time scales in the upper southwest Pacific Ocean. *Journal of Climate*, 18(5), 719–736. <https://doi.org/10.1175/JCLI-3286.1>
- Holbrook, N. J., Goodwin, I. D., McGregor, S., Molina, E., & Power, S. B. (2011). ENSO to multi-decadal time scale changes in East Australian Current transports and Fort Denison sea level: Oceanic Rossby waves as the connecting mechanism. *Deep Sea Research Part II: Topical Studies in Oceanography*, 58(5), 547–558. <https://doi.org/10.1016/j.dsr2.2010.06.007>
- Hristova, H. G., Kessler, W. S., McWilliams, J. C., & Molemaker, M. J. (2014). Mesoscale variability and its seasonality in the Solomon and Coral Seas. *Journal of Geophysical Research: Oceans*, 119, 4669–4687. <https://doi.org/10.1002/2013JC009741>
- Kessler, W. S., & Cravatte, S. (2013a). ENSO and short-term variability of the south equatorial current entering the Coral Sea. *Journal of Physical Oceanography*, 43(5), 956–969. <https://doi.org/10.1175/JPO-D-12-0113.1>
- Kessler, W. S., & Cravatte, S. (2013b). Mean circulation of the Coral Sea. *Journal of Geophysical Research: Oceans*, 118, 6385–6410. <https://doi.org/10.1002/2013JC009117>
- Kessler, W. S., & Gourdeau, L. (2007). The annual cycle of circulation of the southwest subtropical Pacific, analyzed in an ocean GCM. *Journal of Physical Oceanography*, 37(6), 1610–1627. <https://doi.org/10.1175/JPO3046.1>
- Mata, M. M., Wijffels, S. E., Church, J. A., & Tomczak, M. (2006). Eddy shedding and energy conversions in the East Australian Current. *Journal of Geophysical Research*, 111, C09034. <https://doi.org/10.1029/2006JC003592>
- Melet, A., Gourdeau, L., & Verron, J. (2010). Variability in Solomon Sea circulation derived from altimeter sea level data. *Ocean Dynamics*, 60(4), 883–900. <https://doi.org/10.1007/s10236-010-0302-6>
- Pegliasco, C., Chaigneau, A., & Morrow, R. (2015). Main eddy vertical structures observed in the four major Eastern boundary upwelling systems: Eddy vertical structure in the EBUS. *Journal of Geophysical Research: Oceans*, 120, 6008–6033. <https://doi.org/10.1002/2015JC010950>

- Pilo, G. S., Oke, P. R., Rykova, T., Coleman, R., & Ridgway, K. (2015). Do East Australian Current anticyclonic eddies leave the Tasman Sea? *Journal of Geophysical Research: Oceans*, *120*, 8099–8114. <https://doi.org/10.1002/2015JC011026>
- Qin, X., Menviel, L., Sen Gupta, A., & van Sebille, E. (2016). Iron sources and pathways into the Pacific Equatorial Undercurrent. *Geophysical Research Letters*, *43*, 9843–9851. <https://doi.org/10.1002/2016GL070501>
- Qin, X., Sen Gupta, A., & van Sebille, E. (2015). Variability in the origins and pathways of Pacific Equatorial Undercurrent water. *Journal of Geophysical Research: Oceans*, *120*, 3113–3128. <https://doi.org/10.1002/2014JC010549>
- Qiu, B., Chen, S., & Kessler, W. S. (2009). Source of the 70-day mesoscale eddy variability in the Coral Sea and the North Fiji Basin. *Journal of Physical Oceanography*, *39*(2), 404–420. <https://doi.org/10.1175/2008JPO3988.1>
- Qiu, B., & Chen, S. M. (2004). Seasonal modulations in the eddy field of the South Pacific Ocean. *Journal of Physical Oceanography*, *34*(7), 1515–1527. [https://doi.org/10.1175/1520-0485\(2004\)034<1515:SMITEF>2.0.CO;2](https://doi.org/10.1175/1520-0485(2004)034<1515:SMITEF>2.0.CO;2)
- Qu, T., & Lindstrom, E. J. (2002). A Climatological interpretation of the circulation in the Western South Pacific. *Journal of Physical Oceanography*, *32*(9), 2492–2508. <https://doi.org/10.1175/1520-0485-32.9.2492>
- Qu, T. D., & Lindstrom, E. J. (2004). Northward intrusion of Antarctic intermediate water in the western Pacific. *Journal of Physical Oceanography*, *34*(9), 2104–2118. [https://doi.org/10.1175/1520-0485\(2004\)034<2104:NIOAIW>2.0.CO;2](https://doi.org/10.1175/1520-0485(2004)034<2104:NIOAIW>2.0.CO;2)
- Ray, R. D., & Zaron, E. D. (2016). M-2 Internal tides and their observed wavenumber spectra from satellite altimetry. *Journal of Physical Oceanography*, *46*(1), 3–22. <https://doi.org/10.1175/JPO-D-15-0065.1>
- Ridgway, K. R., & Dunn, J. R. (2003). Mesoscale structure of the mean East Australian Current System and its relationship with topography. *Progress in Oceanography*, *56*(2), 189–222. [https://doi.org/10.1016/S0079-6611\(03\)00004-1](https://doi.org/10.1016/S0079-6611(03)00004-1)
- Ridgway, K. R., & Dunn, J. R. (2007). Observational evidence for a Southern Hemisphere oceanic supergyre. *Geophysical Research Letters*, *34*, L13612. <https://doi.org/10.1029/2007GL030392>
- Ridgway, K. R., Dunn, J. R., & Wilkin, J. L. (2002). Ocean interpolation by four-dimensional weighted least squares - application to the waters around Australasia. *Journal of Atmospheric and Oceanic Technology*, *19*(9), 1357–1375. [https://doi.org/10.1175/1520-0426\(2002\)019<1357:OIBFDW>2.0.CO;2](https://doi.org/10.1175/1520-0426(2002)019<1357:OIBFDW>2.0.CO;2)
- Ridgway, K. R., & Godfrey, J. S. (1997). Seasonal cycle of the East Australian Current. *Journal of Geophysical Research*, *102*(C10), 22921–22936. <https://doi.org/10.1029/97JC00227>
- Ridgway, K. R., Godfrey, J. S., Meyers, G., & Bailey, R. (1993). Sea Level Response to the 1986–1987 El-Nino Southern Oscillation event in the Western Pacific in the Vicinity of Papua New Guinea. *Journal of Geophysical Research*, *98*(C9), 16387–16395.
- Roemmich, D., & Gilson, J. (2009). The 2004–2008 mean and annual cycle of temperature, salinity, and steric height in the global ocean from the Argo Program. *Progress in Oceanography*, *82*(2), 81–100. <https://doi.org/10.1016/j.pocean.2009.03.004>
- Rousselet, L., Doglioli, A. M., Maes, C., Blanke, B., & Petrenko, A. A. (2016). Impacts of mesoscale activity on the water masses and circulation in the Coral Sea. *Journal of Geophysical Research: Oceans*, *121*, 7277–7289. <https://doi.org/10.1002/2016JC011861>
- Rykova, T., & Oke, P. R. (2015). Recent freshening of the East Australian Current and its eddies: Freshening of EAC Eddies. *Geophysical Research Letters*, *42*, 9369–9378. <https://doi.org/10.1002/2015GL066050>
- Schütte, F., Brandt, P., & Karstensen, J. (2016). Occurrence and characteristics of mesoscale eddies in the tropical northeastern Atlantic Ocean. *Ocean Science*, *12*(3), 663–685. <https://doi.org/10.5194/os-12-663-2016>
- Souza, J. M. A. C., de Boyer Montégut, C., Cabanes, C., & Klein, P. (2011). Estimation of the Agulhas ring impacts on meridional heat fluxes and transport using ARGO floats and satellite data. *Geophysical Research Letters*, *38*, L21602. <https://doi.org/10.1029/2011GL049359>
- Sprintall, J., Roemmich, D., Stanton, B., & Bailey, R. (1995). Regional climate variability and ocean heat transport in the southwest Pacific Ocean. *Journal of Geophysical Research*, *100*(C8), 15865–15871. <https://doi.org/10.1029/95JC01664>
- Suthers, I. M., Young, J. W., Baird, M. E., Roughan, M., Everett, J. D., Brassington, G. B., et al. (2011). The strengthening East Australian Current, its eddies and biological effects — an introduction and overview. *Deep Sea Research Part II: Topical Studies in Oceanography*, *58*(5), 538–546. <https://doi.org/10.1016/j.dsr2.2010.09.029>
- van Sebille, E., Sprintall, J., Schwarzkopf, F. U., Sen Gupta, A., Santoso, A., England, M. H., et al. (2014). Pacific-to-Indian Ocean connectivity: Tasman leakage, Indonesian Throughflow, and the role of ENSO. *Journal of Geophysical Research: Oceans*, *119*, 1365–1382. <https://doi.org/10.1002/2013JC009525>
- Willis, J. K., & Fu, L.-L. (2008). Combining altimeter and subsurface float data to estimate the time-averaged circulation in the upper ocean. *Journal of Geophysical Research*, *113*, C12017. <https://doi.org/10.1029/2007JC004690>
- Yang, G., Wang, F., Li, Y., & Lin, P. (2013). Mesoscale eddies in the northwestern subtropical Pacific Ocean: Statistical characteristics and three-dimensional structures. *Journal of Geophysical Research: Oceans*, *118*, 1906–1925. <https://doi.org/10.1002/jgrc.20164>
- Yang, G., Yu, W., Yuan, Y., Zhao, X., Wang, F., Chen, G., et al. (2015). Characteristics, vertical structures, and heat/salt transports of mesoscale eddies in the southeastern tropical Indian Ocean. *Journal of Geophysical Research: Oceans*, *120*, 6733–6750. <https://doi.org/10.1002/2015JC011130>
- Yoshida, S., Qiu, B., & Hacker, P. (2010). Wind-generated eddy characteristics in the lee of the island of Hawaii. *Journal of Geophysical Research*, *115*, C03019. <https://doi.org/10.1029/2009JC005417>
- Zhang, Z., Wang, W., & Qiu, B. (2014). Oceanic mass transport by mesoscale eddies. *Science*, *345*(6194), 322–324. <https://doi.org/10.1126/science.1252418>
- Zhang, Z., Zhang, Y., Wang, W., & Huang, R. X. (2013). Universal structure of mesoscale eddies in the ocean. *Geophysical Research Letters*, *40*, 3677–3681. <https://doi.org/10.1002/grl.50736>